The electrochemical reduction of formic acid to methanol

by

Clarissa Louise Gray

Submitted in partial fulfilment of the requirements for the degree

Magister Scientiae

In the Faculty of Natural and Agricultural Sciences

University of Pretoria

Pretoria

2017

Declaration

I, Clarissa Louise Gray, declare that the dissertation, which I hereby submit for the degree Master of Science (Chemistry) at the University of Pretoria, is my own work and has not previously been submitted by me for a degree at this or any other tertiary institution.

SIGNATURE:_____

DATE: _____

Abstract

Four anodic electrocatalytic powders were tested for water electrolysis. Of these a synthesised 70:30 mol% IrO_2:TaC showed the best catalytic activity as it produced the highest current densities at both the stop potential of linear sweep voltammetry and the applied potential during chronoamperometric studies. The onset potential was very similar between all samples ranging between 1.49 and 1.50 V. Field emission scanning electron microscopy showed the emergence of a platy, vitreous-like phase in the synthesised powders with particle agglomerations with rounded edges, increasing the catalytic activity in comparison to commercial IrO_2.

For the reduction of formic acid to methanol experiments, the 70:30 mol% IrO_2:TaC electrocatalyst was used as the anodic electrocatalyst and polyaniline (PANI) as the cathodic electrocatalyst. In eight samples collected from five of the nine membranes which were prepared, methanol was detected by liquid injection gas chromatography. The retention time of methanol varied between 4.62 and 4.97 minutes. This range is attributed to changes made in the gas chromatograph setup between tests. With the increase in applied potential, a higher current density and an increase in the concentration of methanol (%v/v) were observed in samples of the same membrane. The highest production of methanol was found in membrane B2 run at 5.1 V with a concentration of 0.1451 %v/v, this sample produced the highest current density in linear sweep voltammetry experiments, although it only produced the second highest current density for chronoamperometric experiments. This suggests that the catalytic activity for the reduction of formic acid to methanol is not necessarily dependent on the current density produced by the system.

Acknowledgements

First and foremost I would like to thank my supervisor, Dr Shankara G. Radhakrishnan. Thank you for the continued motivation guidance and developing my reasoning abilities. Thank you too for trusting me enough to allow me to make my mistakes in the laboratory and assisting me through them. None of your kindness went unnoticed.

Prof Emil Roduner, thank you for sharing your infectious passion for chemistry with me and asking the questions that kept me searching for more answers.

I'd like to thank my research group, even though we are small and new you kept me on my toes, shared with me your experiences and gave me a good talking to when one was needed.

To my mom, words do not exist that could express my gratitude for all the sacrifices you made while helping me get to where I am now. Yours and Lens patience and love is overwhelming and I am so fortunate to have you cheering me on.

Thank you to my family for being truly interested in my work and for consistently asking me for updates, you made me aspire to learn more so I could explain better.

For my friends who allowed me to bounce my ideas off them during our coffee breaks and for helping me keep my head.

Thank you, Kyle, for being my pillar of strength, listening to my thoughts and giving input when you could. We have travelled an interesting road together and I appreciate every bump and corner.

I am grateful to the National Research Foundation (NRF) and the Swiss-South African Joint Research Programme (SSAJRP) for the funding of this research project.

Contents

List of figures

List of tables

List of abbreviations

Å	Angstrom
A	Ampere
AMP	2-Amino-2-methyl-1-propanol
APUs	Auxiliary power units
Au	Gold
B	Boron
b(2θ)	FWHM in radians
C	Coulombs
CA	Chronoamperometry
CCM	Catalyst
CCR	Carbon capture and recycling
CCS	Carbon capture and sequestration
CGH2	Compressed gaseous hydrogen
CH_4	Methane
CH_3OH	Methanol
cm	Centimetre
cm/s	Centimetre per second
CO	Carbon monoxide
CO_2	Carbon dioxide
$CO_2^{\bullet-}$	Carbon dioxide radical
CO_2RR	Electrochemical CO_2 reduction reaction
CoP21	21st Conference of Parties
Cr	Chromium
C/mol	Charge per mol
DEA	Diethanolamine
DIPA	Di-isopropanolamine
DI water	Deionised water
DMFC	Direct methanol fuel cell
e^-	Electron
e^-_{input}	Electrons put into the system
e^-_{output}	Electrons used by the system to produce analyte
EDX	Energy dispersive x-ray spectroscopy
ET detector	Everhart-Thornley secondary electron detector
F	Faraday's constant (C/mol)
Fe	Iron
FESEM	Field emission scanning electron microscopy
FWHM(rad)	Full width at half maximum height in radians
FWHM(θ)	Full width at half maximum height in degrees
GC	Gas chromatography
GDLs	Gas diffusion layers
GHG	Greenhouse gases
Gm^3	Billion cubic metres
Gt	Billion tonnes
H^+	Proton
HCOOH, H_2CO	Formic acid
HER	Hydrogen evolution reaction
H_2	Hydrogen

$H_2IrCl_6.4H_2O$	Iridic acid
H_2O	Water
I	Current in Amperes
ICEs	Internal combustion engines
*i*PrOH	Isopropanol
Ir	Iridium
IrO_2	Iridium oxide
K	Scherrer constant
kPa	Kilopascal
kV	Kilovolt
kWh/kg	Kilowatt-hour per kilogram
L	Crystallite size in nm
λ	wavelength in nm
LEDs	Light emitting diodes
LH2	Liquefied hydrogen
Li	Lithium
LSV	Linear sweep voltammetry
m	metre
mA/cm^2	Milliampere per square centimetre
MDEA	N-methyl-diethanolamine
MEA	Membrane electrode assembly
MEA	Monoethanolamine
mg	Milligram
Mg	Magnesium
MgH_2	Magnesium hydride
min	minute
MJ/kg	Megajoule per kilogram
MJ/L	Megajoule per litre
mL	Millilitre
mL/min	Millilitre per minute
MΩ	Megaohms
mm	Millimetre
mmol	millimol
Mn	Manganese
Mo	Molybdenum
mol%	Mole per cent
MPa	Megapascal
Mt	Megatonnes
MTO	Methanol to Olefin
Mtpa	Million tonnes per annum
mV/s	Millivolts per second
µL	Microlitre
µm	Micrometre
N	Nitrogen
$NaNO_3$	Sodium nitrate
NO_2	Nitrogen dioxide
N_2O	Nitrous oxide
Nb	Niobium
OER	Oxygen evolution reaction
PANI	Polyaniline
Pd	Palladium
PEM	Proton exchange membrane

PEMWE	Proton exchange membrane water electrolysis
ppm	Parts per million
Pt	Platinum
PTFE	Perfluorinated vinyl ether with tetrafluoroethylene
PXRD	Powder x-ray diffraction
Q	Measured charge in C
Rh	Rhodium
rpm	Revolutions per minute
Ru	Ruthenium
RuO_2	Ruthenium oxide
s	second
Sb	Antimony
SE_2	Secondary electrons
SEM-EDX	Scanning electron microscopy with energy dispersive X-ray spectroscopy
Si	Silicon
Sn	Tin
SPE	Solid phase(polymer) electrolyte
t	Time of experiment in s
Ta	Tantalum
TaC	Tantalum carbide
TEA	Triethanolamine
Ti	Titanium
TVs	Televisions
θ	Bragg angle in degrees
UNFCC	United Nations Framework on Climate Change
USD	United States Dollar
V	Volts
W	Tungsten
WE	Water electrolysis
wt%	Weight per cent
Zr	Zircon
%v/v	Volume of analyte in total sample volume

Chapter 1 Introduction

1.1. Introduction

CO_2 is a greenhouse gas which is cause for concern as it has a long lifetime in the atmosphere. Methods to stabilise emissions by creating a carbon neutral cycle do exist and one of these is the reduction of CO_2 into liquid fuels.

This thesis focuses on the electrochemical reduction of formic acid to methanol on a nitrogen-based organic electrocatalyst. Formic acid is a reaction intermediate in the reduction of CO_2 to methanol and promises an exciting strategy for alternative energy stores for renewables. This investigation was initiated with the development of an experimental method to produce the catalysts and measure the electrocatalytic activity in Chapter 2. In Chapter 3 the results of the water electrolysis and formic acid reduction steps are presented and discussed. Chapter 4 discusses the overall conclusions which were drawn and the possible future works to be carried out on the system.

1.2. Literature review

1.2.1. The urgency to reduce carbon dioxide emissions and atmospheric concentrations

The UN Framework on Climate Change (UNFCC) of 1992 released legislation describing a framework to reduce or stabilise greenhouse gas (GHG) concentrations and emissions in order to prevent the climate system being directly influenced by humans.[1] In 2015 at the 21st Conference of Parties' annual meeting (CoP21) South Africa signed the Paris Agreement. Built into this agreement is ensuring fair participation of all countries in the global effort to reduce GHGs now, and in the future. This also includes ensuring finances are available to fund low carbon or carbon neutral developments.[2,3] In this regard South Africans and the global community are responsible for developing technologies to stabilise or reduce GHG emissions, preferably in a manner that will also provide poverty alleviation.

Carbon dioxide (CO_2), along with methane (CH_4) and nitrous oxide (N_2O) are trace gasses in the atmosphere classified as GHGs. The increasing concentrations of GHGs are responsible for atmospheric changes resulting in global warming. CO_2 is the focus here because CO_2 acts as a thermal barrier which, unlike other GHGs, persists over time.[4] The surge of CO_2 emissions is attributed to the extraordinary rate at which the human population is growing, the standard of living and the use of technology that is on the rise. This results directly in an escalation of deforestation and the burning of fossil fuels, both of which result in a build-up of atmospheric CO_2.[5] In 2014 alone

about 22 million tonnes (Mt) of coal, 12 Mt of oil and 10 billion cubic metres (Gm^3) of natural gas was consumed daily by anthropogenic activities. Of the 30 billion tonnes (Gt) of CO_2 that was released into the environment, half was trapped in the atmosphere as it couldn't be absorbed by plants or the ocean (a major sink for CO_2).[4,6]

As the current worldwide average CO_2 concentration surpassed the 400 ppm mark in 2016, it cannot be denied that the "Anthropocene", an epoch where anthropogenic activities are having a major, long lasting impact on the planet, has been entered into.[5] This had also been described as "the point of no return" because of the long lifetime of CO_2 and scientists are unsure of what lies ahead.[7,8] This shows that anthropogenic activities have already affected the global climate system which was what the UNFCC attempted to prevent. Hence, we not only need a very drastic decrease in current emissions but further need to recycle emissions and extract CO_2 from the atmosphere. The production of CO_2 can't be prohibited as was successfully accomplished with chlorofluorocarbons and hence another solution is required.[9] The only available technologies that can achieve this in significance is through Carbon Capture Sequestration (CCS) or Carbon Capture and Recycling (CCR).[3,9]

CCS is the large scale storage of CO_2 in underground cavities.[3] CO_2 is trapped from "large point sources"[10] which include fossil fuel power plants, fuel processing plants, and other industries. Iron, steel, cement and bulk chemicals manufacturing industries account for 50% of anthropogenic CO_2 emissions.[6,10,11] CO_2 has been stored in both onshore and offshore environments in depleted gas fields, geological basins and offshore deep saline formations and basins associated with CO_2 enhanced oil recovery.[3] However, storing CO_2 underground has its own dangers: slow leakage or quick release when a nearby geological event occurs.[9] CCS has been extensively researched and is already quite mature and in commercial use with 22 large-scale CCS projects in operation or under construction, with the capacity to capture 40 million tonnes per annum (Mtpa) of CO_2.[3,10] The South African government has indicated that a commercial scale CCS plant will be commissioned by 2025.[12] However the drawback to this technology is that captured CO_2 is not reused but rather just stored and there will be a constant struggle to find new storage areas.

Disposal of CO_2 is illogical as it is not only expensive and an energy rich process but for each tonne of CO_2 disposed of, approximately 0.4 – 0.5 tonnes are generated.[10]

CCR is the harnessing of CO_2 which has been trapped from the abovementioned large point sources and then recycled.[10] Three methods have been described for the recycling of CO_2 which are: the conversion of CO_2 into liquid fuels, the use of CO_2 as a feedstock for chemicals, and enhanced

biological fixation[10]. For example, CO_2 may be reduced to methanol, other single and higher hydrocarbon fuels, and polymers.[13,14]

In both CCS and CCR, atmospheric CO_2 concentrations will be greatly reduced but only in CCR will the CO_2 be made of further use in industrial or leisure settings while at the same time ensuring a carbon neutral cycle. It has recently been proven that CO_2 can be captured from air.[15] This may lead to technologies in the future that will allow for CO_2 to be captured from small sources like households etc.[6]

The conversion of CO_2 to liquid fuels, specifically the electrocatalytic reduction of CO_2 to methanol, is the main inspiration for this research. As such the methanol economy, advantages and disadvantages thereof, as well as the electrocatalytic reduction to methanol, are discussed hereafter.

1.2.2. The methanol economy

Essential to humankind's current way of life are the fossil fuels burned and the oil and natural gases used. These non-renewable resources do not only provide power but are often also the origin of many materials and products that are heavily relied on.[16] New sources of energy need to desperately be invented and utilised. This can be provided by numerous renewable sources, such as solar or wind, but not on the scale large enough to completely replace fossil fuels, yet.[16] Another problem with renewable energies is the storage of the energy produced in order for it to be available on demand. Many of the renewable technologies only operate under specific conditions, for example, solar power can only harness energy during daylight and peak household consumption is after dark. However, there are technologies to choose from, with a plethora of battery designs, supercapacitors, storage of energy in chemical bonds including hydrogen and hydrogen carrier liquid fuels, pumped hydro and compressed air storage etc. all of which may fulfil a specific niche.[9,17]

Nobel laureate, George Olah, introduced the concept of a "methanol economy" as opposed to the much popular "hydrogen economy". He first defined the obstacles faced by the hydrogen economy; these will be mentioned as well as types of hydrogen store discussed hereafter.

The production of hydrogen itself is currently a fossil fuel based process[6] this is via syn-gas production followed by the reverse water-gas-shift reaction. This produces CO_2 as shown below. C^* may either be coal, oil or methane.

Syn-gas reaction: $C^* + H_2O \rightarrow CO + H_2$

Water-gas-shift-reaction: $CO + H_2O \leftrightarrow CO_2 + H_2$ [6]

There is a need for infrastructure development for the transport and commercial use of hydrogen as a fuel source.[16] Hydrogen may also be produced by water electrolysis (WE) an environmentally friendly process. WE requires no fossil fuels if the energy is provided by renewables or photoelectrodes, and doesn't produce CO_2.[18]

Possible means of hydrogen storage present themselves in physical and chemical storage. Physical storage is the most mature technology thus far and includes compressed gaseous hydrogen (CGH2), liquid storage (LH2) and cryo-adsorption.[19]

Hydrogen is incredibly volatile and flammable[16,20] and needs to be compressed to be a sufficient energy carrier otherwise the storage density is just too low. The optimum pressures for compression are within the range 35-70 MPa. This has been the best option for automotive applications to date. Liquefied hydrogen, on the other hand, has a massive advantage in that it has a high mass density but at 0.1 MPa and -253℃. This in itself brings its disadvantages: as heat enters the storage unit from the surroundings evaporation of hydrogen occurs which builds up pressure in the tank so the tank needs to be vented resulting in loss of hydrogen. Furthermore, to maintain the required temperature, multilayer vacuum superinsulation is needed and the wrapping of these foils is highly demanding. In order to liquefy hydrogen there is a 30% loss of stored chemical energy during the cooling process and specialised containers are needed to store the liquefied hydrogen.[16,20,21] However, if liquefied hydrogen is to be used for large volume storage the evaporation losses are not critical.[19]

No adsorbents have the energy density required at ambient temperature and pressure they need to be cooled (cryo-adsorption). These systems need constant cooling from liquid nitrogen which involves a large cost but may still be practical for large stage storage. Adsorbents include zeolites, various carbon materials, polymers with intrinsic microporosity (PIMS), and metal organic frameworks (MOFs). The disadvantage of adsorptive systems is the low volumetric density.[19]

There are various forms of chemical storage, not all of which will be covered here. Hydrides which consist of hydrolytic systems whereupon reaction with water releases hydrogen and a metal (hydr)oxide is formed. The drawback to these systems is that each time the hydrogen is released, it would need to be replenished at the plant which is both costly and energy intensive. These systems are hard to control but $NaBH_4$ has shown some promise and may still find use in remote power supplies. In contrast, in metal hydrides the hydrogen fills interstitial spaces, however not fully. There are two types of metal alloys that can be used, the first is of the type AB_5 (LiN_5) which is very

expensive but has a good storage capacity at 0.2 MPa and ambient temperature, the second is of the type AB_2 (A = Ti, Zr, Mg and B = Cr, Fe, Mn) these do not have as good storage capacity but are implemented in fuel cell systems with solid state hydrogen storage. It has been suggested to pressurise metal hydrides to increase their storage capacity however this will add a lot of weight to the system. As a metal hydride, MgH_2 is a good candidate, it has a good hydrogen storage capacity, material costs are low and there is good reversibility during the cycling process. Complex hydrides have hydrogen covalently bonded to a metal (or non-metal in the case of boron) to form a metal anion. The storage capacity thereof depends on the molar mass of the metals and the number of hydrogens bound to it. Aluminium hydrides have been the focus area in this regard. Materials based on all three types of hydrides show promise of achieving higher storage capacity in the future.[19]

The focus is now shifted to liquid fuels as hydrogen stores, hydrogenation/dehydrogenation of cyclic hydrocarbons, reforming of liquid hydrocarbons and especially reforming of methanol. Hydrogenation/dehydrogenation of cyclic hydrocarbons (also known as organic hydrides) has been intensely discussed and are proposed to fulfil the gap in supply and demand of renewable energies during seasonal changes or for fuel-cell powered cars where dehydrogenation would occur at the hydrogen filling station.[19,22,23] The drawback to this technology is that for rehydrogenation of the aromatic compound it will need to be sent back to a plant.[19]

Liquid hydrocarbons may be reformed although some of these are already used as fuels as is, they have good volumetric and gravimetric energy densities (dependant on the hydrocarbon). A large amount of research is currently ongoing in the field of auxiliary power units (APUs) or remote power source. This has a distinct advantage over batteries due to higher power densities.[19]

Methanol, also considered a hydrogen store due to its relatively good volumetric energy density, is primarily being produced via non-green methods, via syn-gas production followed by a water-gas-shift-reaction to produce syn-gas. The syn-gas is then converted to methanol which requires high pressure and low temperatures. Methanol may also be produced by the reforming of methane by various methods.[6,19] These methods are not sustainable and this echoes the fact that an environmentally friendly manner to produce methanol must be found. This may be via the reduction of CO_2. This exists as: the catalytic hydrogenation of CO_2 which is efficient enough to have already established pilot plants in Japan and Iceland; photocatalytic reduction; electrochemical reduction at either high or ambient temperatures; and finally biomass and waste based processes.[24,25]

Many of the abovementioned processes of forming methanol have resulted in a mixture of products namely: carbon monoxide; formic acid; formate; formaldehyde; dimethyl ether; methyl methanoate; methane; and methanol among others. All of these are still valuable products which themselves may be used as fuels or easily converted to methanol via a secondary process. [6,16]

Methanol is used directly as a liquid fuel in Direct Methanol Fuel Cells (DMFCs) and due to its high octane number it can be mixed with petrol and used in internal combustion engines (ICEs). Methanol is also used as a refrigerant, solvent, and a feedstock to the chemical industry. Methanol can be used to produce light olefins and other hydrocarbons in the Methanol to Olefin process (MTO). Methanol may also replace liquefied petroleum gas or liquefied natural gas as energy sources. [6,9,24]

The volumetric energy density of compressed hydrogen gas at 700 bar is slightly more than 5 MJ/L, liquefied hydrogen is approximately 10 MJ/L and methanol about 15 MJ/L.[26] In this case methanol is the best, however the reverse is true if the gravimetric energy densities are compared: Hydrogen (in all forms) has a gravimetric energy density of 120 MJ/kg whereas methanol fails in comparison at only 20 MJ/kg. The figure below illustrates this visually. Methanol's energy density (both volumetric and gravimetric) is approximately half that of petrol (gasoline).[27]

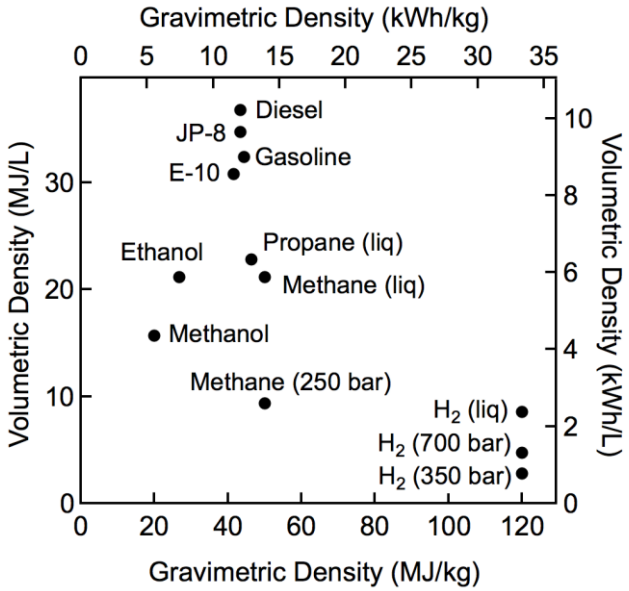

Figure 1: Volumetric and gravimetric energy densities of various fuels.[27] The energy densities if methanol and various forms of hydrogen may be compared to that of diesel and gasoline.

1.2.3. Electrochemically catalysed reduction of CO_2 to methanol

1.2.3.1. Background

Although there has been research on the electrochemical reduction of CO_2 for a few decades it had not shown any possibility of successful transition to industry, recently this has changed and is quickly gaining momentum. Chemically, the largest hurdle to overcome in this process is the inherent stability of the CO_2 molecule. This is the most stable form of carbon - a fully oxidised linear molecule which requires a large amount of energy to destabilise it to a radical intermediate ($CO_2^{\bullet -}$). This radical is proposed to be the intermediate necessary to allow reaction of CO_2 on metal electrodes but is not definite in organic systems. We, therefore, need to develop techniques to produce an efficient, robust catalyst and methods which minimise this energy required for conversion. Renewables will provide this energy and in such the process will be carbon neutral.[6,28–30]

Other processes which can convert CO_2 to valuable products were mentioned above and include thermochemical processes which generally require high pressure and temperature and H_2 as a reducing agent. Photochemical processes are also available whereby illuminated semiconductor electrodes are used as photoanodes to supply electrons to a dark cathode or a photocathode which directly reduces CO_2, currently, the selectivity and/or production rates are too low.[28,30]

Advantages associated with electrochemical reduction over other methods are: the reaction can take place in ambient conditions; the source of energy is renewables resulting in a carbon neutral process; the setup including electrode, applied energy and electrolyte may in future be tuned to obtain a specific desired product, examples of which exist.[6,28,30]

There are inherent disadvantages to the method of electroreduction of CO_2 as well. There is a very high energy barrier that needs to be overcome to activate CO_2 to the proposed reactive intermediate $CO_2^{\bullet -}$ which requires a large potential of about 1.90 V. A larger than theoretically required potential will need to be applied because of various types of dissipation, charge transfer overpotentials and cell resistances. The potential required just for the reaction to the radical ion (assuming the reaction goes via this process) is larger than the overall cell potential for the reduction of CO_2 to methanol at a standard cell potential of 1.21 V. Due to sluggish kinetics and limited mass transfer the reaction rates are slow, this results in low conversion rates and current densities. Oftentimes mixed products result as the onset potentials to various products are relatively close to each other (see the tables below) and separation thereof is required post reduction. Other than that when using an aqueous electrolyte the reaction competes with the Hydrogen Evolution Reaction

(HER) because it occurs at a similar standard cell potential (1.23 V). The reduction of CO_2 is much more complicated than water electrolysis and as such it is difficult to determine a reaction pathway especially with non-conventional metal and non-metal catalysts.[6,28,30,31]

Table 1: Standard potentials for CO_2 reduction

Half-cell reaction	E^0 (V)
$CO_2 + 2H^+ + 2e^- \rightarrow CO + H_2O$	- 0.10[6,32]
$CO_2 + 2H^+ + 2e^- \rightarrow HCOOH$	- 0.11[6,32]
$CO_2 + 4H^+ + 4e^- \rightarrow H_2CO + H_2O$	- 0.028[6]
$CO_2 + 6H^+ + 6e^- \rightarrow CH_3OH + H_2O$	+ 0.031[6]
$CO_2 + 8H^+ + 8e^- \rightarrow CH_4 + 2H_2O$	+ 0.17[6]

Table 2: Standard potentials for intermediate reactions

Half-cell reaction	E^0 (V)
$HCOOH + 2H^+ + 2e^- \rightarrow H_2CO + H_2O$	- 0.03[32]
$H_2CO + 2H^+ + 2e^- \rightarrow CH_3OH$	+ 0.24[32]
$CH_3OH + 2H^+ + 2e^- \rightarrow CH_4 + H_2O$	+ 0.58[32]

Solutions need to be found to the challenges of low efficiencies and mixed products to realise this technology in the industrial sector. An electrocatalytic reduction of CO_2 reactor needs to be compact and easily scaled up on demand. In other words the poor performance of core components specifically the electrocatalyst needs to be eliminated and the reaction must reach a current density of at least 100 mA/cm^2.[6,30] This technology can easily be kept compact by using solid polymer electrolytes (SPE) as opposed to conventional liquid electrolytic systems and specific to this research: proton exchange membranes (PEM).

1.2.3.2. Proton exchange membrane and general membrane electrode assemblies

SPEs were first introduced in the 1950s during the Space Race when there was a need for a safer fuel cell system, one without corrosive electrolytes which could leak and would boil in the vacuum of space. Solid electrolytes found their uses here, and in the 1960s E.I. du Pont Co. invented a more chemically and mechanically robust membrane, Nafion®. Nafion® is a copolymer of perfluorinated vinyl ether with tetrafluoroethylene (PTFE) which could be used in electrolysis cells.[31,33] The chemical structure is as follows, although others have been shown too:

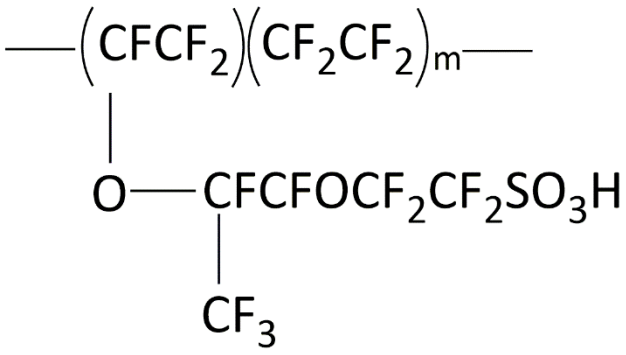

Figure 2: Chemical structure of Nafion[33]

The morphology and physical structure of Nafion® have been and continue to be extensively studied, with many proposed models. A feature common to all these models is that the ionic group aggregates in the perfluorinated polymer matrix. This forms a network of clusters which allows for significant swelling by polar solvents. The clusters of ionic groups allow for efficient ion transport through these nanometer domains – hence Nafion® must have some degree of hydration to be active. The geometry and spatial distribution of the ionic clusters is also still debated, it has been shown that the hydrophilic and hydrophobic phases do not present themselves in discrete domains.[33]

These membranes allow for separation between the cathodic and anodic compartments of electrolysis and fuel cells, whilst keeping the electrodes relatively close to each other (Nafion® 117 has a typical thickness of 0.178 mm), such to reduce electrical resistances and overall cell potential. They have a high proton conductivity (approximately equivalent to 1 M H_2SO_4), excellent mechanical stability, good chemical stability as they allow for the passage of protons and not electrons, thereby they are chemically neutral and have low gas solubility and permeability. This is crucial to prevent oxygen crossover which would result in re-oxidation of the products at the anode. In comparison to

regular electrolysis cells, electrolysis cells containing SPE can operate at higher current densities and have much lower ohmic resistances than those with liquid electrolytes.[9,30,31,33]

Industrially they have the added advantages of being stacked, largely decreasing space required for reactors and can operate efficiently at fairly high current densities (approximately 1 A/cm^2).[24,30]

Despite the low permeability of Nafion® this still exists and leads to some issues. With electro-osmotic drag, permeability allows mass transfer through the membrane. The electroosmotic drag of water with protons from the anodic to cathodic compartments reduces liquid flow at the anodic and increases volume at the cathodic compartment. The amount of water dragged by a proton is proportional to the current density, temperature and indirectly proportional to the water content. Between 1 and 4 water molecules per proton (drag coefficient) have been reported to accompany a proton as it crosses over.[24,33,34]

The membrane electrode assembly used in this study resembles that for PEM water electrolysers, fuel cells and direct methanol fuel cells (DMFC). The setup varies very slightly but in general consists of a PEM (Nafion® 117) with the cathode and anode electrocatalysts on either side, followed by gas diffusion layers/electrode (GDL/E), current collectors and finally, the anode and cathode compartments.[30] Chapter 2, Figure 3 shows a graphic representation of this membrane electrode assembly.

An electrocatalytic ink is prepared by mixing the electrocatalytic powder with a PTFE solution, adding a solvent (such as isopropanol) and a binding agent (ethylene glycol, glycerine etc.). The ink has to be left stirring thereafter to stay in suspension. This electrocatalytic ink is used in multiple ways. It may be sprayed directly onto the PEM,[35] in some cases is further hot pressed between GDLs. The ink may also be sprayed onto the GDLs directly.[18] The electrocatalyst can also be dry pressed onto the GDLs and the entire MEA is hot-pressed thereafter.[36] These variations in MEA preparation are an attempt to make the system as efficient as possible by bringing the electrocatalysts and the PEM as close to each other as possible and in such, decreasing mass transport losses.[30,35] There are also cases where the electrocatalyst ink is coated onto a glassy carbon electrode – this is to test the effectiveness of an electrocatalyst and not in a system as a whole[37,38].

GDLs are porous and hydrophobic, the structure thereof ensures the entire electrocatalyst is used and increases the interface between the gas, electrocatalyst and electrolyte. In layman's terms, they are used to increase the solubility and dispersion of gases (CO_2) as they approach the electrocatalyst whilst preventing the pores of the electrocatalyst being flooded by water as this would inhibit gas

transport. In such, increase mass transport and efficiency of the system.[39,40] This makes them a crucial component in the MEA of an electrolysis cell.

Chapter 2 Materials and Methods

2.1. Preparation of anodic electrocatalyst powders

The preparation of the anodic catalyst powders was based on the procedure described by Polonsky *et al.*[41], an adapted Adam's Fusion Method[37,42]. Here a metal chloride precursor is fused with excess $NaNO_3$ at high temperature.[42] Since its invention, this method has been used to prepare various metal oxides[37,42,43]. In this study, iridic acid ($H_2IrCl_6{\cdot}4H_2O$, Alfa Aesar, 99 %, Ir 38-42 %) was the metal precursor and tantalum carbide (TaC, Aldrich, ≥5 µm, 99 %), the support material. During preparation, the amounts of iridic acid used changed between samples but the necessary amount of TaC was adjusted to keep the ratios as they needed to be as shown in the table below.

Table 3: Amount of reagents used to make anodic electrocatalytic powders

Ratio IrO_2:TaC (mol%)	**Sample no.**	**$H_2IrCl_6{\cdot}4H_2O$ (g)**	**TaC (g)**	**$NaNO_3$ (g)**
100:0	100 HM	0.0590	-	0.0701
70:30	70:30	0.0522	0.0037	0.0637
	Anode powder 01	0.1809	0.0126	0.2140
	Anode powder 02	0.1838	0.0128	0.2178
	Anode powder 03	0.1843	0.0128	0.2174
60:40	60:40	0.0554	0.0059	0.0665

During the course of the research slight modifications were made to the method as deemed necessary but followed closely by the following procedure. Iridic acid was weighed into a crucible, to this TaC was quantitatively transferred from wax paper using a portion of 10 mL isopropanol (*i*PrOH, Sigma-Aldrich, HPLC 99.9 %). The remainder of the *i*PrOH was poured into the crucible and left to stir (Lasec digital hotplate stirrer) for 1 hour. Excess (approximately 16.7 molar) $NaNO_3$ (Sigma-Aldrich, ≥99 %) was added to the mixture and heated to 70 °C using a digital thermometer until a sludge formed. The stirrer bar was removed and the crucible placed in the furnace (Carbolite) which was heated to 500 °C at 250 °C/hr, left to dwell at 500 °C for one hour and allowed to cool to room temperature overnight. The resulting dark grey-black powder was scraped into a centrifuge tube with 6 mL deionised (DI) water (Millipore Synergy, 18.2 MΩ) and centrifuged (Heraeus Sepatech, Labofuge 200) at 2600 rpm three times, decanting the supernatant and refilling with water each time. The powder was then washed using a Millipore® Sterifil® filtration system with Millipore® filter paper (HTTP type, 0.4 µm diameter) and left to dry overnight.

2.2. Treatment of Nafion® 117 membrane

The Nafion® membrane (Alfa Aeser, N-117) was cut into a 4 cm x 4 cm piece, rinsed with DI water and lightly boiled in a 3% H_2O_2 (Alfa Aesar, 35% w/w) solution for about an hour. Thereafter it was rinsed in DI water and placed in lightly boiling DI water for approximately two hours. It was then lightly boiled in a 0.5M H_2SO_4 (Merck, 95 – 99%) solution for around one hour and stored in DI water until needed.[44]

2.3. Preparation of electrocatalytic ink and catalyst coated membrane

Preparation of the electrocatalytic ink was based on that by Sun *et al*[35]. For each 100 mg electrocatalytic powder, 0.6 mL of Nafion® perfluorinated resin solution (Aldrich, 5 wt% in lower aliphatic alcohols and water) was added and left to stir for an hour. Thereafter approximately 4 mL *i*PrOH was added, stirred for fifteen minutes and left to sonicate (Emerson, Branson 1800 ultrasonic bath) on high for an hour. To this, for each 100 mg catalyst powder, 0.25 mL ethylene glycol (Sigma-Aldrich, spectrophotometric grade ≥99%) was added and sonicated for a further hour. The resulting suspension was left to stir until use.

The pre-treated Nafion® membrane was tapped dry with Kimwipes* (Kimtech Science* brand delicate task wipes), placed on a clean pane of glass and secured with tape (Scotch™ Magic™ Tape) to reveal only a 2 cm x 2 cm surface area for catalyst spraying. A portion of the suspension was pipetted into the paint reservoir of the airbrush (Conrad Electronic Airbrush-Pistole AB-200) and sprayed directly onto the 2 cm x 2 cm area. During spray coating, swelling occurred due to the hydrophobicity of the membrane and the membrane was left to return to normal before spraying continued. The entire suspension was used per membrane.

In the case of water electrolysis testing, only the one side of the membrane was coated with the anodic electrocatalytic ink. However, for the formic acid (Sigma-Aldrich, reagent grade, ≥ 95%) tests, the anodic electrocatalyst was sprayed on first, left to dry overnight, and the following day the membrane was turned over and the cathodic electrocatalyst was sprayed on. In both cases the membranes were left for at least 24 hours to dry before being activated in a lightly boiling 0.5 M H_2SO_4 solution for approximately two hours, rinsed and stored in DI water until use.

After the first few membranes, it proved too difficult to tape off a precise area without touching the membrane excessively, so a piece of silicone rubber (National Instruments) with a 2 cm x 2 cm cut out in the centre was placed over the membrane and secured to the glass pane with tape.

When reactivating two of the membranes, some of the electrocatalyst peeled off. It was unclear why this happened and the membranes were prepared again.

Table 4 below shows the size of the active area as well as catalyst coating per square centimetre. All membranes for the formic acid reduction tests used synthesised 70:30 mol% IrO_2:TaC as the anodic electrocatalyst. Membranes A, B, and C were the first three prepared before it was taken into account to use a constant mass of electrocatalytic powder. These samples had compositional variations in the anodic electrocatalytic ink: for A the anodic ink was made of 70:30 mol% commercial IrO_2:TaC powders which were mixed together prior to adding perfluorinated resin and then followed the method as set out above was used, for B the synthesised 70:30 mol% IrO_2:TaC powder was used and C used a 50:50 mass ratio of synthesised anodic powder and Vulcan (Fuel cell store, XC72) for the ink. For all other membranes a 70:30 mol% synthesised IrO_2 was used and prepared in an identical fashion in an attempt to produce identical membranes. Membranes 4 to 6 were prepared with one batch of ink, three times the usual amount, the membranes were placed on the glass, taped together to allow approximately 2 cm x 2 cm area of each membrane to be visible and sprayed.

Table 4: Loading of electrocatalytic powders on membranes

Membrane name	Size of active area (cm^2)	Mass anodic electrocatalyst powder used (mg)		Loading of anodic electrocatalyst powder on membrane (mg/cm^2)	Mass cathodic electrocatalyst powder used (mg)		Loading of cathodic electrocatalyst powder on membrane (mg/cm^2)
Water electrolysis							
100	4	14.4		3.6	-		-
70:30	4	10		2.5	-		-
60:40	4	14.4		3.6	-		-
Formic acid reduction							
A	4	6.3		1.6	5.4		1.4
B	4	14.1		3.5	21.1		5.3
C	4	14.7		3.7	6.5	3.3 Polyaniline 3.2 Vulcan	1.63
B1	4	14.4		3.6	5.6		1.4
B2	4	14.5		3.6	5.3		1.3
B3	4	14.5		3.6	5.4		1.4
B4	3.61	43.7	12.7	3.5	16.5	4.8	1.3
B5	3.99		14.0	3.5		5.3	1.3
B6	4.83		17	3.5		6.4	1.3

2.4. The membrane electrode assembly

2.4.1. Electrode assembly for water electrolysis

Titanium screen mesh cloth (Fuel Cell Store, Product number 592782) was used as the GDL on the anode side, sandwiched between the catalyst coated membrane and a silicone gasket. On the cathode side a platinum coated carbon cloth (0.3 mg/cm^2 40% on Vulcan – carbon cloth electrode, Fuel Cell Store, Product number 1610002) was used as a catalyst coated GDL, followed by a silicone gasket and titanium mesh current collectors which came with the fuel cell casing (Fuel Cell Store, E105). This was followed by the outer casing which had a serpentine groove spanning 2 cm x 2 cm each with an inlet and outlet point to a well containing DI water as depicted graphically in Figures 3 and 4.

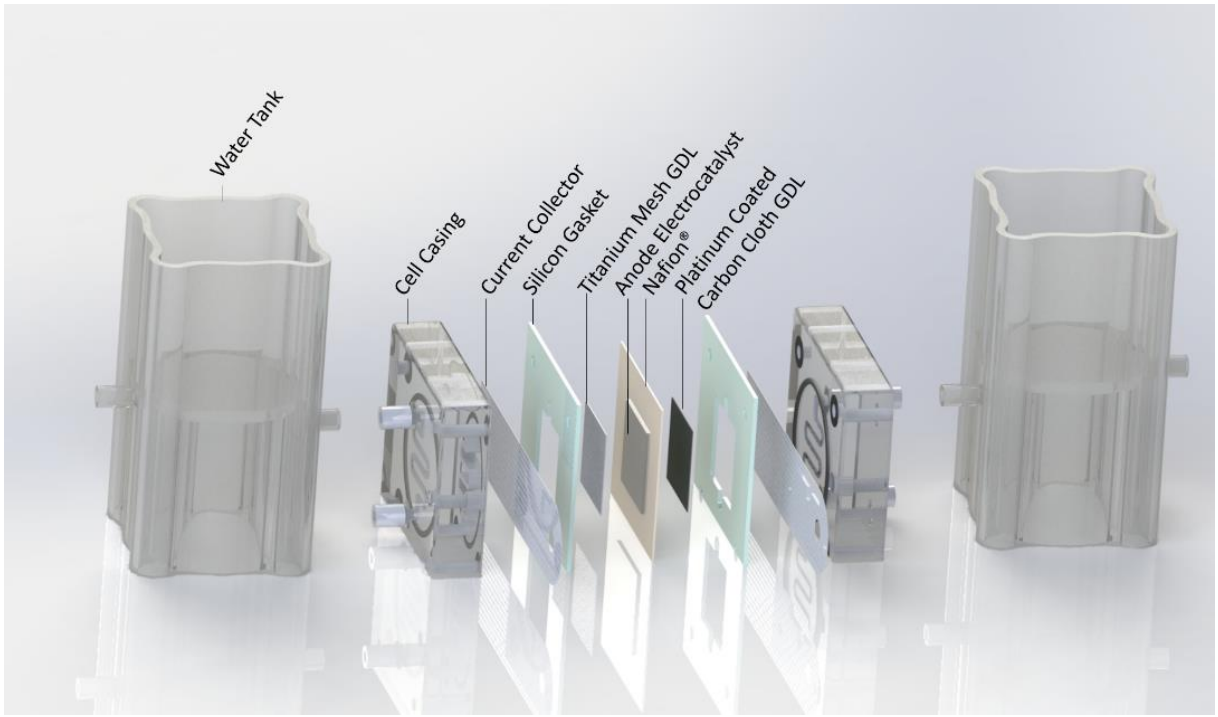

Figure 3: Cell set-up including the membrane electrode assembly. For the formic acid reduction, the cathodic electrocatalyst was coated on the backside of the membrane the platinum coated carbon cloth was replaced with untreated carbon paper, and the cathodic well was replaced with a glass cylinder.

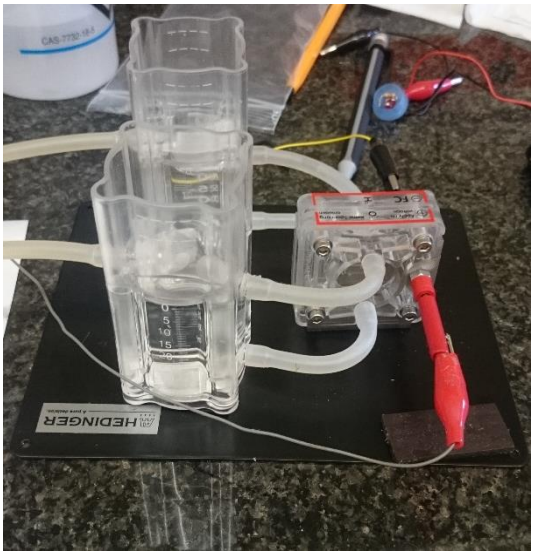

Figure 4: Membrane electrode assembly for water electrolysis. For the formic acid reduction, the well on the cathode side was replaced with a glass cylinder.

2.4.2. Electrode assembly for formic acid reduction

The double-sided CCM was sandwiched between two different GDLs: a Ti coated mesh on the anode and untreated carbon paper (Alfa Aesar, TGP-H-60) at the cathode, both followed by silicone gaskets, Ti current collectors and finally the outer cell casings. A plastic well containing DI water sat at the anode side and a glass cylinder with an open top containing formic acid at the cathode side.

2.5. Potentiostatic measurements

Measurements were performed in a 2-electrode cell on a potentiostat/galvanostat (Autolab, AUT72638) running Nova 2.0 and later 2.1 software. Linear sweep voltammetry (LSV) was conducted with a scan rate of 1 mV/s and a step potential of 0.1 V, depending on the experiment the end potential range differed. Chronoamperometric (CA) studies were also conducted at various potentials as shown in the table below. Only the samples in which methanol was detected are shown.

Table 5: Membrane and sample name with experimental conditions

Membrane name	Sample name	Experimental conditions
Water electrolysis		
100		LSV 40 runs -0.1 – 2.1 V CA 12 hours @ 2.1 V
70:30		LSV 40 runs -0.1 – 2.1 V CA 12 hours @ 2.1 V
60:40		LSV 40 runs -0.1 – 2.1 V CA 12 hours @ 2.1 V CA 12 hours @ 1.9 V
Formic acid reduction		
B		LSV 40 runs -0.1 – 2.6 V CA repeat x 10 : 5 min @ 1.9 V 5 min @ 2.1 V CA 30 min @ 2.6 V LSV 10 runs -0.1 – 2.6 V
		LSV with $N_{2(g)}$ flowing over anode 7 runs -0.1 – 2.6 V
	B	Followed on with same formic acid sample LSV after $N_{2(g)}$ 10 runs -0.1 – 2.6 V
B1	B1_15% formic acid	LSV 20 runs -0.1 – 2.6 V CA 48 hours @ 2.6 V CA 48 hours @ 1.9 V CA 6 hours @ 2.1 V
B2	B2_15% formic acid	LSV 20 runs -0.1 – 2.6 V CA 24 hours @ 2.6 V CA 24 hours @ 1.9 V CA 12 hours @ 2.1 V
B3	B3_3.1 V	LSV 10 runs -0.1 - 3.1 V CA 24 hours @ 3.1 V
	B3_4.1 V	LSV 10 runs -0.1 – 4.1 V CA 24 hours@ 4.1 V
	B3_5.1 V	LSV 10 runs -0.1 – 5.1 V CA 24 hours @ 5.1 V
B4	B4_3.1 V	LSV 6 runs -0.1 – 3.1 V CA 24 hours @ 3 V
B5	B5_5.1 V	LSV 6 runs -0.1 – 5.1 V CA 24 hours @ 5 V LSV 2 runs -0.1 – 5.1 V
B6	B6_4.1 V	LSV 6 runs -0.1 – 4.1 V CA 24 hours @ 4 V LSV 2 runs -0.1 – 4.1 V
	B6_5.1 V	LSV 6 runs -0.1 – 5.1 V CA 24 hours @ 5 V LSV 2 runs -0.1 – 5.1 V

The average run and standard deviations were calculated in Origin Pro 2016 using its “Statistics on row” feature where descriptive statistics were performed on the sample. Grubb’s test was performed on the terminal current densities for a set of LSV runs to determine whether there were any outliers. If an outlier was found in the terminal current densities then the penultimate current

densities were also tested. If there remained an outlier then that run was removed from the calculation of the average.

2.6. Characterisation

2.6.1. Powder x-ray diffraction

For powder x-ray diffraction (PXRD) all powder patterns for the electrocatalytic powders were collected using a Bruker D2 Phaser powder diffractometer at room temperature. CuK-α radiation was generated at 30 kV and 10 mA with a wavelength, $\lambda = 1.54$ Å. Patterns were collected in a range from 5 – 45° 2θ in steps of 0.05° and a counting time of 2 seconds per step. There was very little of each sample so the fine sample powders were evenly sprinkled onto a low background silicon quartz sample holder. Origin Pro 2016 was used to subtract the background of the recorded diffractograms and the matching of the components within the powder was carried out on Diffrac.Eva software (version 2.0).

2.6.2. Field emission scanning electron microscopy with energy dispersive x-ray spectroscopy

A Zeiss Ultra 55 (Germany) field emission scanning electron microscope (FESEM) was used to observe the morphology of samples of the electrocatalytic powders, used and unused coated Nafion® membranes. These were mounted on double-sided carbon tape by either dipping the stubs into the powders or cutting a small piece of the catalyst coated membrane (CCM) and sticking it onto the tape. Excess powder was removed by blowing compressed nitrogen gas over the sample. None of the samples were sputter-coated as they were conductive. The analysis was carried out at 1 kV with the standard in-lens detector and for some samples, an Everhart-Thornley secondary electron detector (SE2) was used at 4 kV. Energy dispersive x-ray spectroscopy (EDX) was also conducted on the anode powders to observe the distribution of Ir versus Ta as well as the surface concentration.

2.6.3. Gas chromatography

Gas chromatography (GC) analysis was performed on all liquid and some gas samples to detect any formaldehyde, methanol or methane produced. This was carried out on a customised Agilent G1530A 6890 gas chromatograph with a split injection port controlled by a two position actuator module - VICI (Valco Instruments Co. Inc.). Helium gas was used as the carrier gas. The conditions are given in the table below.

Table 6: GC conditions

Column type I	Zebron 7HG-G007 -11 ZB-WAX column
Column diameter	250 µm
Column film thickness	0.25 µm
Mode	Constant flow
Initial flow	1.2 mL/min
Average velocity	40 cm/s
Inlet	
Heater	250 °C
Pressure	62.9 kPa
Total flow	28.1 mL/min
Detector	Flame ionisation detector fitted with a methaniser (nickel catalyst)
Heater	250 °C
Hydrogen flow	40.0 mL/min
Air flow	450 mL/min
Electrometer	On
Column type II	Carboxen -1006 PLOT Capillary
Column diameter	320 µm
Column film thickness	15 µm
Mode	Constant flow
Initial flow	3.0 mL/min
Average velocity	47 cm/s
Inlet	
Heater	200 °C
Pressure	116 kPa
Total flow	156 mL/min
Detector	An analogue input board (AIB) was used to connect a pulsed discharge ionisation detector (PDHID)
Oven	
Initial	40 °C for 7 min
Ramp	230 °C at 20°C/min

For liquid samples a clean syringe (Hamilton-Bonaduz, MICROLITER® #7002) was rinsed 15 times with the liquid sample, discarding each time, followed by 15 rinses while keeping the needle in the solution to prevent any bubbles forming. A 2 µL sample was taken and injected into the front liquid inlet. For gas samples, the syringe (VICI precision sampling, Inc., Pressure-Lok®) was pumped three times with ambient air then rinsed three times with the gaseous headspace of the liquid sample,

held on the third time for twenty seconds to allow for equilibration. A 30 mL sample was injected into the gas sample valve.

Chapter 3 Results and discussion

3.1. Anode electrocatalyst for oxygen evolution reaction

3.1.1. Background

Proton Exchange Membrane Water Electrolysis (PEMWE) was originally invented to produce electrolytic grade oxygen in anaerobic environments.[45] There were distinct advantages of this technology over the previously used alkaline process, namely: electrolysers were more compact and they could be stacked, at higher current densities they were more efficient, operated better under pressure and, in turn, storage or removal of the by-product, hydrogen, was made easier.[45]

With the birth of the concept of the "Hydrogen Economy", PEMWE was considered to produce clean hydrogen, however, reforming from methane became the preferred method at that time as it was cheaper.[45] Currently, with the increase of greenhouse gas emissions, especially CO_2, as well as global awareness on climate change, a carbon neutral, environmentally friendly technology to produce hydrogen has seen PEMWE become popular in research again.[45,46]

The current disadvantage of PEMWE is the need for both the anodic and cathodic electrocatalysts to be made of noble metals or their oxides.[46–48] However, because only the anode is applicable to this research, only the anode will be considered from here on out. The trend in the electrocatalytic activities for noble metals is as follows: Ru ≈ Ir > Pd > Rh > Pt > Au > Nb.[49,50] For noble metal oxides RuO_2 had shown the best activity, followed closely by IrO_2. However, RuO_2 oxidises further in the harsh environment at the anode and IrO_2 has shown much better stability and hence is more commonly researched.[41,51–53] IrO_2 has shown to increase the stability of RuO_2 even at a low concentration of 20 wt%.[51] Both of these metal oxides have a rutile structure where the metal cations are octahedrally surrounded by the oxygen anions.[48] RuO_2 and IrO_2 have the best activities due to their high metallic conductivity. This is attributed to the overlap of the metal-metal distances which allow for the overlap of the inner d-orbitals. It is these inner d-orbital electrons which are responsible for electron conduction.[47] Another perspective is that the main conduction band is formed by the overlap of the metal t_{2g} and oxygen p-orbitals.[48]

From the literature, it is apparent that IrO_2 is the favoured noble metal oxide under research but due to its low crustal concentration and high demand (for example use in automobiles and LEDs for smartphones, tablets, TVs), it is very highly priced. In the last five years, Iridium prices have ranged

between 400 to 1 000 USD per troy ounce.[54] For this reason, it has become imperative for researchers to reduce catalyst loading, which is usually done by introducing a support or composite material, and also discovering cheaper, noble metal free or even metal free electrocatalysts.[18,55–57]

In an effort to keep expenses low, research into metal free OER electrocatalysts has increased drastically compared to that of metal oxides with support material. Notable examples are carbon based electrocatalysts because carbon is a crustal abundant element, much cheaper and has already seen use as electrocatalysts.[55,57] Unfortunately, their stability at the anode surface as well as the electrocatalytic activities toward OER does not supersede that of IrO_2, yet.[55] Recently, it has been discovered that doping of carbon with heteroatoms, especially nitrogen, significantly improves the activity of these electrocatalysts with quaternary and pyridinic nitrogens as the active sites.[56,58] On account of their low activities these materials were not considered for the anodic electrocatalyst.

A support or composite material is a non-reactive material which must be both inexpensive and readily available.[41] The task of the support is to: i) decrease the loading (amount) of the more expensive active material; ii) increase the number of crystallisation centres available for the active material during deposition (this results in a smaller crystallite size of the active material and prevents agglomerations to ensure better homogeneity of the active material); iii) the supported particles are larger than unsupported particles which is a massive advantage if the electrocatalyst is applied directly onto the gas diffusion layer (GDL) because the particles will not penetrate deeply into the GDL resulting in less wastage of the electrocatalyst and more area for activity; iv) there may also be synergism between the active material and the support which would promote electrochemical activity.[18,41,53,59]

As previously mentioned, IrO_2 is the best noble metal oxide for OER as it has good activity coupled with high stability[49–52] and because of this, it was chosen as the active material for this study. In order to reduce the amount needed, a support needed to be introduced and the type thereof chosen. Some of the supports which have been tested in laboratory PEMWE setups include: IrO_2 + Nb_2O_5[60], SnO_2 + IrO_2 + Ta_2O_5[61], $Ir_xRu_yTa_zO_2$[62], IrO_2 + SnO_2[52,59,63], and IrO_2 + TaC[18,41]. Others have been tested in a conventional electrolysis cell by deposition onto a titanium substrate: Ti/IrO_2 + Ta_2O_5[64], and Ti/IrO_x + Sb_2O_5 + SnO_2[65].

On a side note, it was long believed that the support material should be conductive as well but Mazur *et al*[53] showed that a non-conductive TiO_2 support showed synergetic effects with the IrO_2 active material.

The use of SnO_2 as a support material has had mixed results[52] whereas TaC has specifically demonstrated a significant enhancement of the activity of the electrocatalyst[18,41]. Polonsky *et al*[41] tested four ceramic based materials for use as a support material: TaC, Si_3N_4, WB, and MoB_5. These were all exposed to conditions harsher than those found at the anode surface of the OER and TaC was concluded to be the most resilient, in fact, it showed no signs of degradation or instability. These reasons are why TaC was chosen as the support material for this study.

A later study by Polonsky *et al*[18] was used in this research to prepare and test the anodic electrocatalyst. Polonsky used a modified Adam's fusion method to prepare the electrocatalyst and found the emergence of a third phase, $NaTaO_3$, a non-conductive layer formed due to the oxidation of TaC by $NaNO_3$, which repressed the activity of the electrocatalyst. They tested various compositions of IrO_2:TaC from 100:0 to 0:100 wt% and changed the concentrations in increments of 10 wt%. From these experiments, they concluded that $NaTaO_3$ had less effect after a concentration more than 50 wt% IrO_2 with the best results at 70:30 wt% which even showed better performance than IrO_2 alone.[18]

The Adam's fusion was first described by Adams and Shriner[42] for the preparation of PtO_2 from platinic acid in the presence of molten nitrate. Modified versions of this method have been used extensively to prepare noble metal oxides from metal acid precursors and is a relatively easy method which gives high yields.[18,53,66,67] It has been suggested and widely accepted that the following chemical reaction takes place with regard to IrO_2:

$$H_2IrCl_6 + 16NaNO_3 \rightarrow NaCl + Ir(NO_3)_4 + 2HNO_3$$

$$Ir(NO_3)_4 \rightarrow IrO_2 + 4NO_2 + O_2$$

IrO_2 precipitates out as $NO_{2(g)}$ is evolved.

Other methods used to prepare noble metal oxides include the polyol method which involves the reduction of a metal precursor in ethylene glycol followed by thermal oxidation. The sol-gel method is also used, however when the solvent is removed there is a chance that the precursor type may affect the properties of the material. Thermal and chemical oxidation of metal colloids may be carried out directly.[66]

PEMWE technology was used in this study and as such, one of its biggest drawbacks, the oxygen evolution reaction (OER) akin to PEMWE[68] needed to be discussed, and a suitable material for the anode chosen and tested before any efforts were made to find a suitable cathode material for CO_2 (or formic acid) reduction experiments.

3.1.2. Results and discussion

3.1.2.1. Field emission scanning electron microscopy

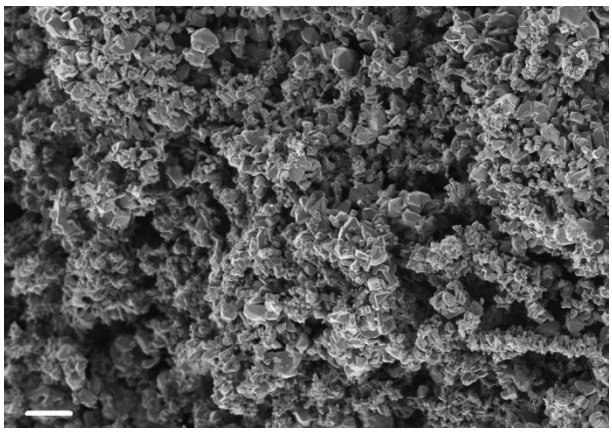

Figure 5: FESEM image of commercial IrO_2. Size bar 1 µm

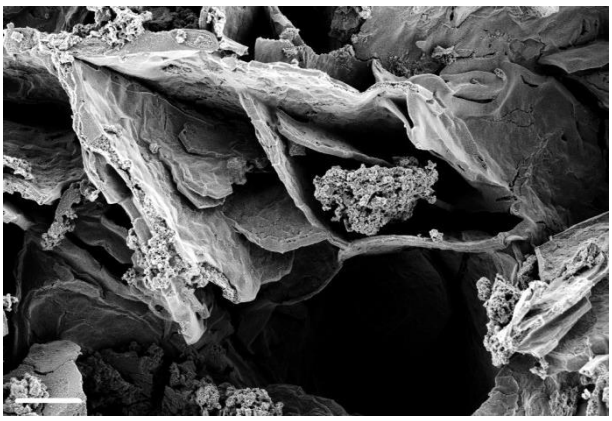

Figure 6: FESEM image of synthesised 100 % IrO_2. Size bar 2 µm

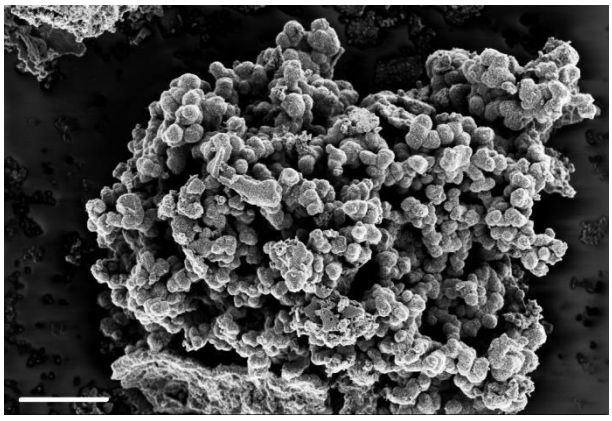

Figure 7: FESEM image of synthesised 100 % IrO_2. Size bar 2 µm

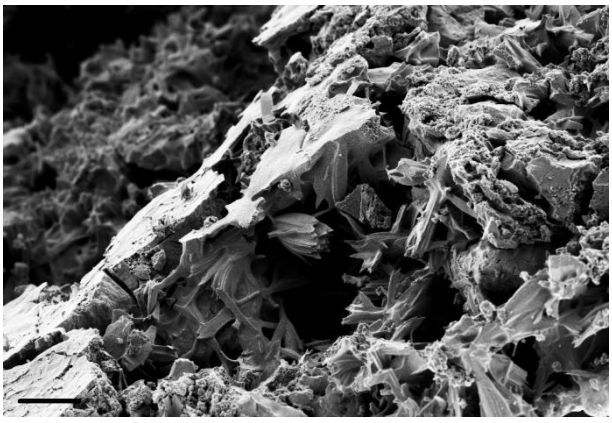

Figure 8: FESEM image of synthesised 70:30 mol% IrO_2:TaC. Size bar 2 µm

Figure 9: FESEM image of synthesised 70:30 mol% IrO_2:TaC. Size bar 2 µm

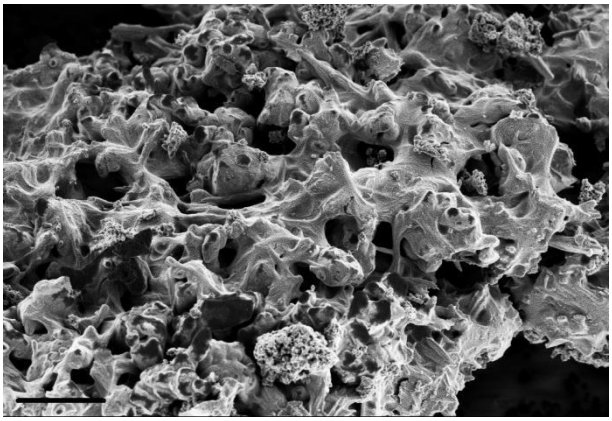

Figure 10: FESEM image of synthesised 60:40 mol% synthesised IrO_2:TaC. Size bar 2 µm

FESEM was used to gauge the morphology of the commercial and synthesised anodic electrocatalytic powders to compare similarities and differences between them which may affect the electrocatalytic activity.

The micrograph of commercial IrO_2 (figure 5) shows nanoparticle agglomerations. These particles have sharp edges and are in the range of 1 µm. In comparison to the synthesised pure IrO_2 there are some distinct differences. Firstly, for the synthesised IrO_2 as seen in figure 6, a platey, vitreous-like phase emerged with nanoparticle agglomerations scattered along the surface, these particles vary in size, also in the range around 1 µm. This platiness causes the surface of the electrocatalyst to be more uneven in comparison to the commercial IrO_2, which also increases the surface area of the electrocatalyst and hence the area available for electrocatalytic activity. Figure 7 shows an area of agglomerated synthesised IrO_2 with a high concentration of particles with rounded rather than sharp edges like those of the commercial sample. This indicates that the surface area to mass ratio is relatively high thus promoting electrocatalytic activity[41]. The platey, vitreous-like structure is common in all the synthesised electrocatalytic powders but becomes more pronounced with the increase in TaC concentration, when comparing figures 6, 8, and 10, with no apparent differences in the number of agglomerations.

Figure 9 shows an anomaly amongst the micrographs. There doesn't seem to be a vitreous-like layer, instead, the platiness shows improved definition and on top of this structure, particle agglomeration occurs more frequently. However, this wasn't observed at any other site or in any other sample. This signifies inhomogeneity in the morphologies of the powders, at least to some extent.

The disadvantage of FESEM analysis is that one is only analysing a very small, possibly uncharacteristic sample of the electrocatalytic powder. At least three different sites were inspected in an attempt to ensure the micrographs were characteristic of the sample as a whole.

3.1.2.2. Energy dispersive x-ray spectroscopy

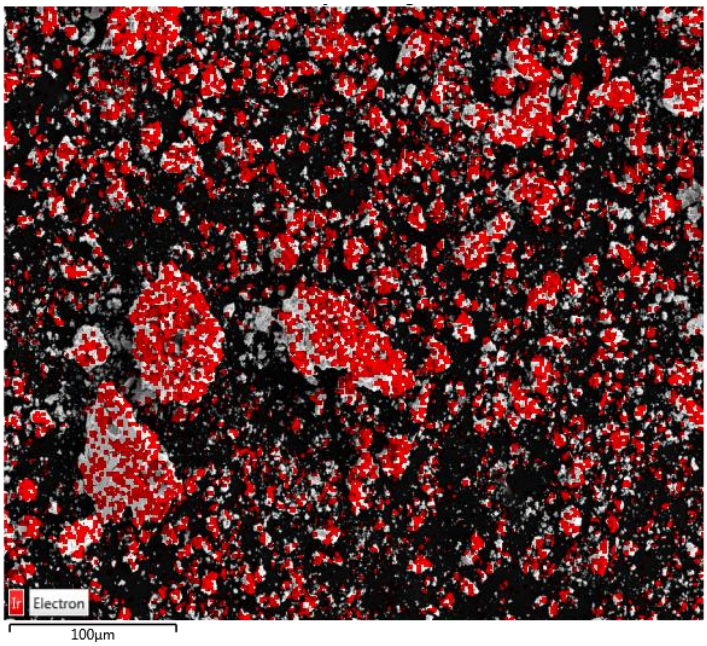

Figure 11: SEM-EDX map for 100% IrO_2 synthesised, IrO_2 indicated by red. Size bar 100 µm

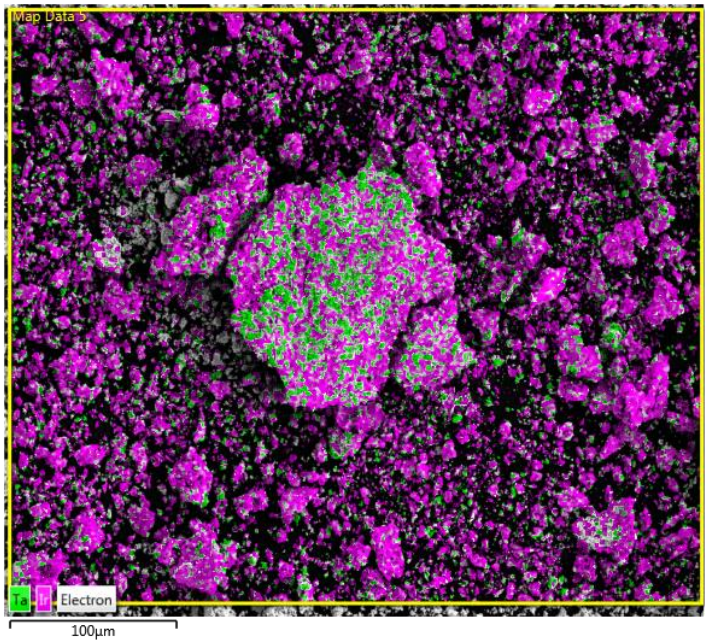

Figure 12: SEM-EDX map for 70:30 IrO_2:TaC, IrO_2 indicated by purple and TaC by green. Size bar 100 µm

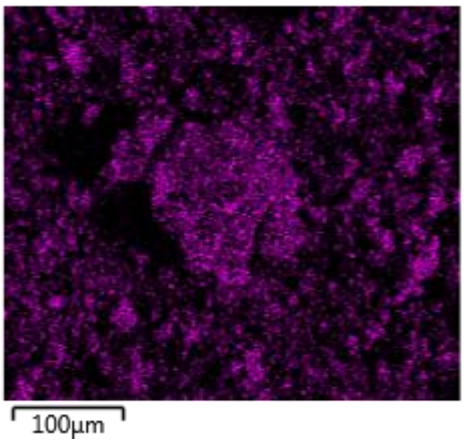

Figure 13: SEM-EDX map of IrO_2 series for 70:30 IrO_2:TaC, size bar 100 µm.

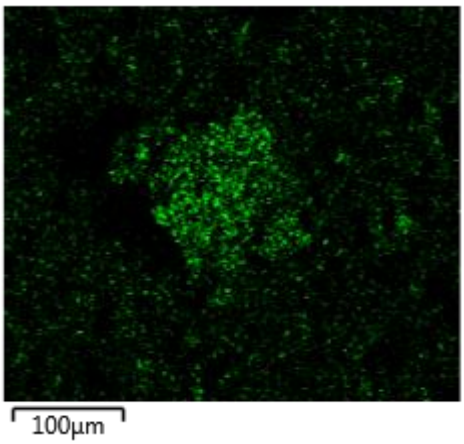

Figure 14: SEM-EDX map of TaC series for 70:30 IrO_2:TaC, size bar 100 µm.

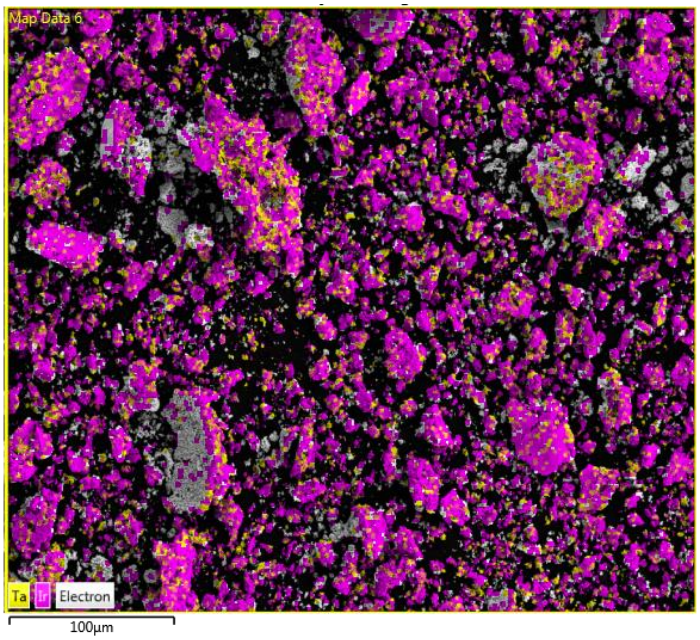

Figure 15: SEM-EDX map for 60:40 IrO_2:TaC, IrO_2 indicated by purple and TaC by yellow. Size bar 100 µm

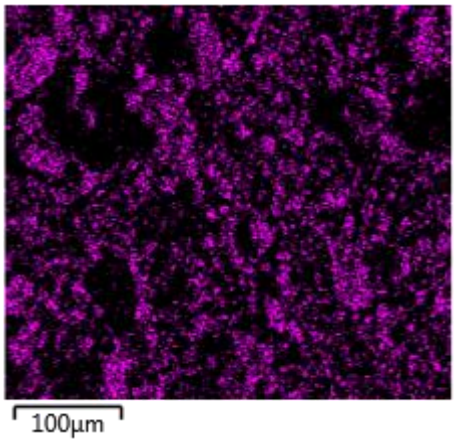

Figure 16: SEM-EDX map for IrO_2 series of 60:40 IrO_2:TaC, size bar 100 µm.

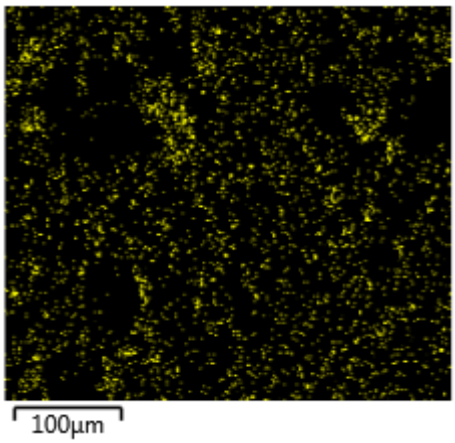

Figure 17: SEM-EDX map of TaC series for 60:40 IrO_2:TaC, size bar 100 µm

Figures 11, 12 and 15 show excellent homogeneity in the electrocatalytic powders throughout the sample. In the SEM-EDX series figures for both 70:30 and 60:40 samples (figures 13, 14, 16, and 17), homogeneous distribution of both Ir and TaC is observed, this correlates well to literature[41]. It also appears that for both samples there is less Ta than Ir, noted by the intensity of the colours, where in both cases the purple which indicates IrO_2 is much more pronounced, this suggests a surface enrichment of IrO_2.

For the mass sum spectra (given in Appendix A) only Ir and Ta were selected as possible candidates. This is because if carbon was selected as a possible species, it would give incorrect results due to the sample preparation, as the powders were applied onto carbon tape (described in Chapter 2). For pure IrO_2 the map sum spectrum shows 100 wt% Ir as expected but in both the 70:30 and 60:40 samples the surface concentration of Ir is 90 wt%. This affirms what was observed in the SEM-EDX figures and that there is in fact surface enrichment of IrO_2.

The FESEM and SEM-EDX findings conclude that there is an overall homogeneity in the distribution of the electrocatalyst and its support with only minor observable differences in morphologies. The synthesised 100% IrO_2 has a morphology better suited for catalytic purposes due to its round edges. Once TaC is introduced a new platy, vitreous-like phase is formed which may contribute to the electrocatalytic activity.

3.1.2.3. Powder x-ray diffraction

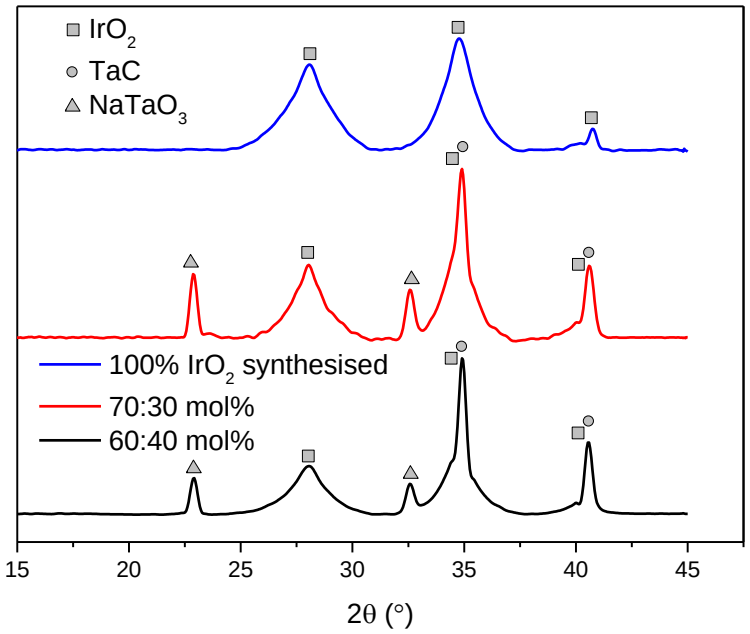

Figure 18: X-ray diffractograms of anodic electrocatalytic powders synthesised for PEMWE tests. Shapes correspond to characteristic peaks of the components as shown.

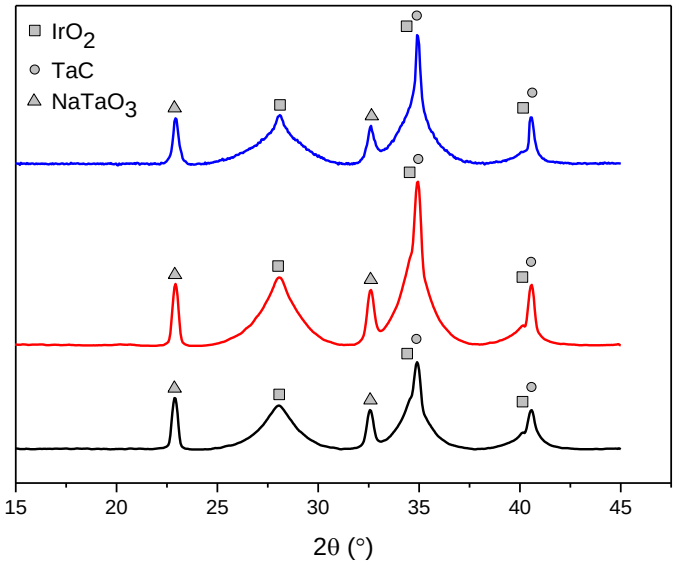

Figure 19: Overlay of PXRD patterns of the anodic electrocatalytic powder diffraction patterns of all the anodic powders used in the formic acid reduction experiments. Black is anode powder 01, red is anode powder 02, and blue is anode powder 03.

Figures 18 and 19 above show the components of the synthesised anodic electrocatalytic powders. All display the characteristic IrO_2 peak at 2θ = 28° which describes the [1,1,0] crystal plane.[41] There is an overlap of the TaC and IrO_2 peaks at 2θ = 35 and 41° because the peaks are positioned too closely and are too broad to be resolved properly. The skewness of the peaks indicates the presence of two different components. There is an emergence of a third component during the modified Adam's fusion method when TaC is added as the support material which is assigned $NaTaO_3$ and is the product of the oxidation of TaC by $NaNO_3$. [41]

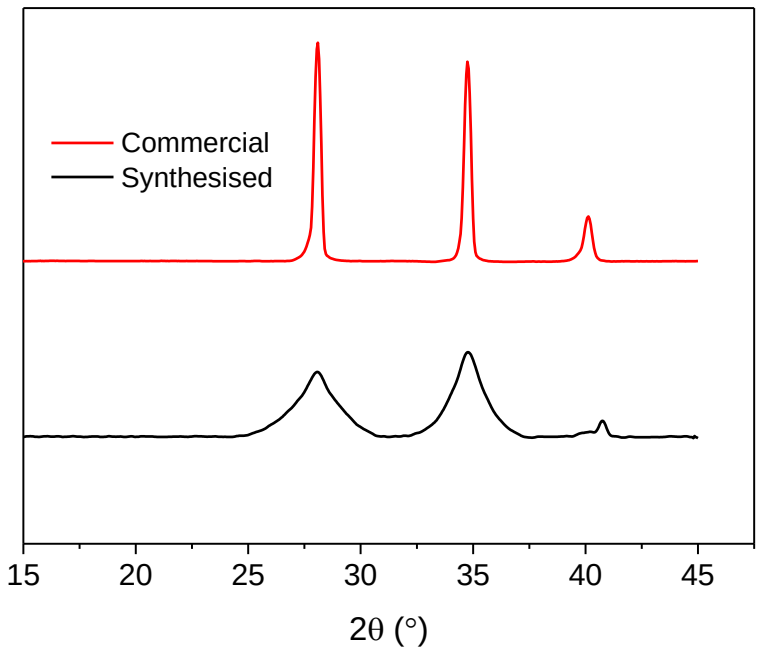

Figure 20: PXRD diffractogram comparing commercial and synthesised IrO_2 (100%).

The commercial and synthesised IrO_2 diffractograms exhibit peaks at the same 2θ values. The differences between the two are the resolution of these peaks as well as the peak height, both of these factors are more pronounced in the commercial sample. This suggests better crystallinity of the IrO_2 crystallites.[43] In other words not only may the crystallites be smaller but may also have fewer lattice defects.

Table 7 Average crystallite size (L) of anode samples for water electrolysis determined by the Scherrer equation.

IrO_2:TaC mol%	FWHM (θ)	FWHM (rad)	2θ (°)	cosθ	L (nm)
100:0 commercial	0.33544	0.0058545	28.0977	0.0882022	270
100:0 synthesised	2.23902	0.0390783	28.0469	0.113472	31
70:30	1.81328	0.0316477	28.0469	0.113472	39
60:40	1.97137	0.0344069	28.0469	0.113472	36

The crystallite sizes can be calculated by the use of the Scherrer equation given by equation 1:

$$L(nm) = \frac{K \cdot \lambda(nm)}{b(2\theta) \cdot cos\theta} \quad \ldots 1$$

where *L* is the crystallite size, *K* is the Scherrer constant (shape factor) taken to be 0.9 because the full width at half height (FWHM) method was used and the crystallite shape is not truly known, λ is the wavelength of the CuK-α radiation, *b(2θ)* is the FWHM of the peak in radians, and θ is the Bragg angle in degrees.[69–71]

As determined by the Scherrer equation, the crystallite sizes of the synthesised electrocatalytic powders are in the range of 31 to 39 nm. 100% IrO_2 has the smallest crystallite size, followed by 60:40 IrO_2:TaC, and lastly 70:30 IrO_2:TaC. This trend is exactly opposite to the literature reported values[41] and the crystallite sizes are almost tenfold larger. Therefore, the 70:30 IrO_2:TaC wt% had the smallest crystallite size, followed by 50:50 and finally 100 IrO_2 wt%. They did not perform tests on a 60:40 ratio and it is also important to note that their ratios were wt% and not mol%, however, there is not a significant difference between these (70:30 mol% = 73:27 wt%). The crystallite sizes of all synthesised electrocatalytic powders are smaller than the commercial crystallite size by almost a factor of ten.

Although using the Scherrer equation is a good approximation of crystallite size, it cannot be considered absolute. The crystallite size is inversely proportional the broadness of the peak but there are more factors which may contribute to peak broadening rather than just the crystallite size. These factors may be due to lattice defects and include dislocations, stacking faults, twinning, micro stresses, grain boundaries, sub-boundaries, coherency strains and, point defects[72]; or it may even suggest a slightly amorphous nature of the IrO_2[43].

The crystallite sizes calculated from the Scherrer equation are in the nm range where we see the particle size of the agglomerations in the FESEM micrographs in the µm range this may suggest that the particles are viewed in FESEM and definitely not the crystallites. The increase in the calculated crystallite size in comparison to literature[41] may be due to the emergence of the platey phase observed in the FESEM images which may not only increase the amorphous nature of the electrocatalytic powders but would also increase the crystallite size and hence the breadth of the peaks in the diffractograms.

3.1.2.4. Electrochemical characterisation

3.1.2.4.1. Linear sweep voltammetry

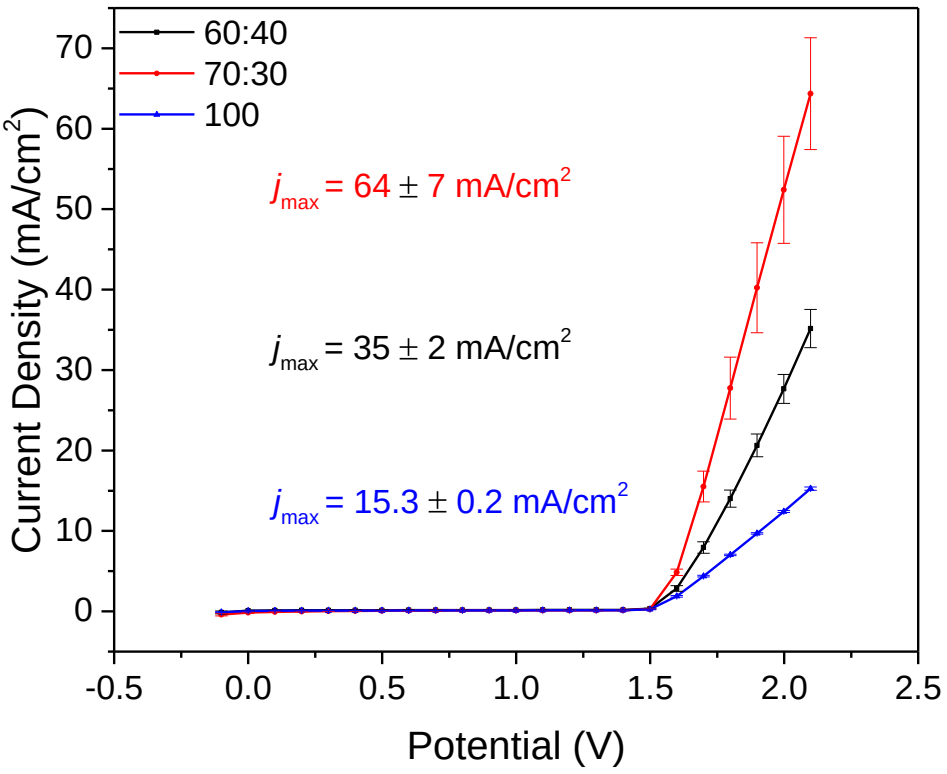

Figure 21: Linear sweep voltammogram for water electrolysis with current density values quoted at 2.1 V.

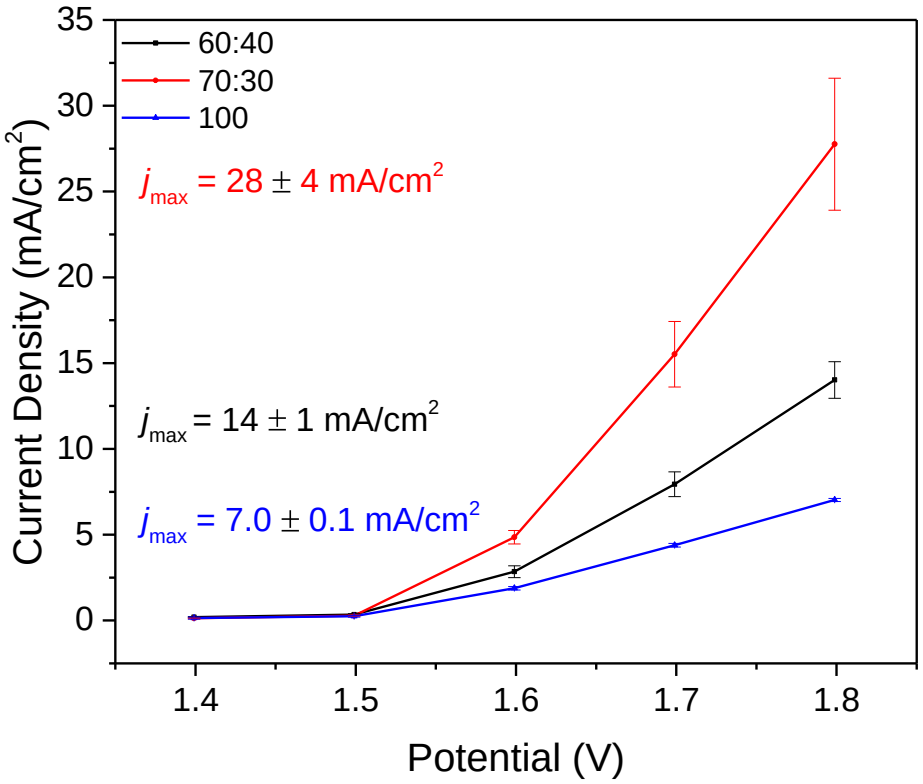

Figure 22: Linear sweep voltammogram for water electrolysis from 1.4 to 1.8 V, current densities at 1.8 V.

Linear sweep voltammetry was conducted on the three various IrO_2:TaC anodic electrocatalysts during water electrolysis to identify the onset potentials, as well as the maximum current density at the stop potential of 2.1 V.

The voltammograms in figures 21 and 22 above graphically demonstrate the average current densities each sample achieved in a run of 40 linear sweep voltammetry (LSV) cycles from -0.1 to 2.1 V, figure 21 is a portion of the voltammogram from 1.4 to 1.8 V. 70:30 IrO_2:TaC is clearly the best sample of the three achieving the best current densities of 64 ± 7 mA/cm^2 at 2.1 V and 28 ± 4 mA/cm^2 at 1.8 V. What may also be noted from the above is that the higher the current density, the more the variation there is in current densities over the 40 cycles as depicted by the standard deviations.

Figure 22 is given here to make the data comparable to the work of Polonsky *et al*[18] where, at 1.8 V Polonsky reached much higher current densities, in the range of 1.00 to 1.50 A/cm^2, while this wasn't achieved in the current study. The appreciable differences between the two methods that may have resulted in the differences in data are that Polonsky spray-coated the electrocatalytic ink

directly onto the GDL whereas in this study it was spray-coated onto the Nafion® and because the ink was coated onto the GDL, the catalyst loading was accurately determined. Whereas, with the hydrophobic nature and moisture sensitivity of the membrane, the determination of the catalyst loading was not as accurate. In literature[18] the compartments were also pressurised to 300 kPa whereas, in this study, all our experiments were carried out at ambient pressure (approximately 100 kPa). Pressurising the chambers ensured the water stayed as liquid and by not pressurising the chambers, gas bubbles formed as hydrogen and oxygen formed at both the cathode and anode respectively. As long as these bubbles remained in the serpentine grooves, the reaction was not running at maximum efficiency and this may have resulted in, not only the lower current densities but may have contributed to the variances between the cycles of a specific run. Here all experiments were also carried out at ambient temperature whereas in literature[18] the water was heated before it entered the chambers. Heating the water gives it energy which would have activated the reaction.

There are similarities in the shape of the voltammograms where literature describes two regions.[18] Firstly, a region where the current increases in an exponential fashion and the charge transfer is the rate limiting step. Secondly, the current densities increase linearly with the potential and this has been attributed to the ohmic resistances in the cell with the membrane contributing to the majority. This is the region in which PEMWE are operated at in the industrial setting and is influenced by the conductivity of the electrocatalyst.[18] These two regions are also observed in the voltammograms for this study with 70:30 IrO_2:TaC having the highest slope in the second region and hence better performance of the electrocatalyst in the PEMWE than the other two samples.

At lower potentials, there is very little differences between the three samples and the onset potentials were incredibly similar, 1.50 V for 100% IrO_2 and 1.49 V for 60:40 and 70:30 samples, only 190 and 180 mV above the theoretical onset potential for water electrolysis which is 1.21 V.

3.1.2.4.2. Chronoamperometry

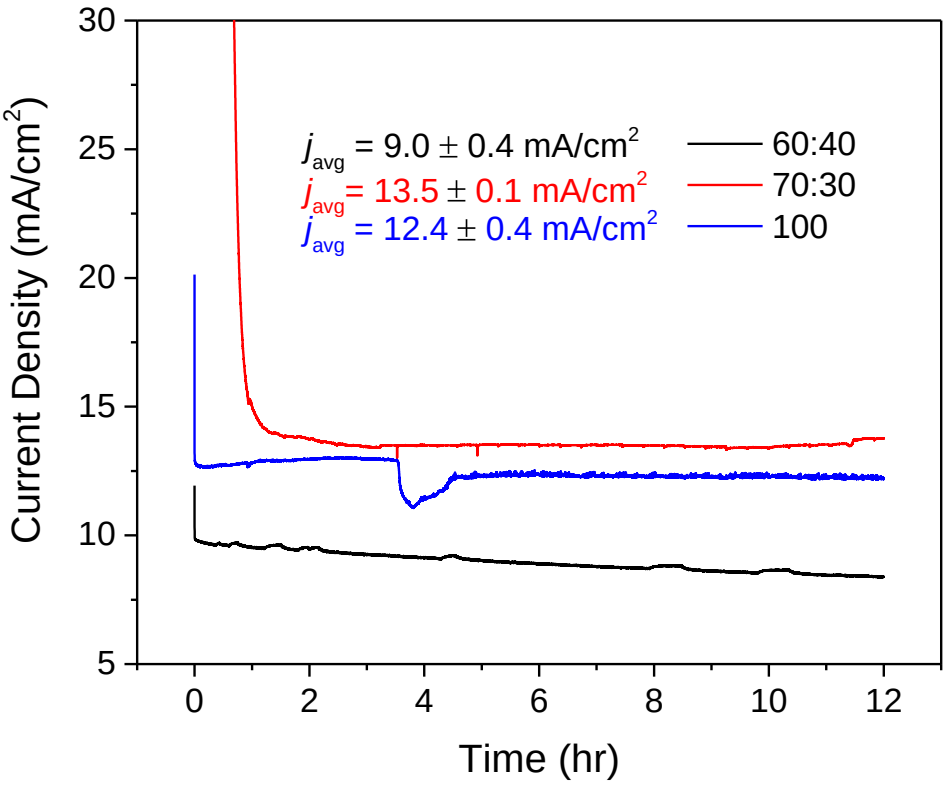

Figure 23: Chronoamperometry for water electrolysis.

In order to determine whether the electrocatalytic coated membranes were stable under long running times, constant potential chronoamperometric studies were conducted on each sample for twelve hours. The hump in the 100 % sample at around four hours is because the setup was moved slightly during the run. All samples show constant current density during the run by the horizontal straight line, indicating good stability over the twelve hour period. The initial quick decrease in the beginning of the run is due to the charging current. Again, 70:30 IrO_2:TaC showed the best performance at 13.5 ± 0.1 mA/cm^2, a very constant current density over the twelve hour period.

From all the experiments 70:30 mol% IrO_2:TaC showed the best results and was thus used as the anodic electrocatalyst in all consequent experiments. All samples showed good homogenous distribution between the active and support material with similar morphologies. PXRD was an adequate tool to use for the characterisation of the electrocatalytic powder composition.

3.2. Cathode electrocatalyst for formic acid reduction reaction

3.2.1. Background

At present, the challenge is to find a suitable cathodic electrocatalyst for the electrochemical CO_2 reduction reaction (CO_2RR) to methanol, or other liquid fuels. This catalyst will: fixate CO_2 on the electrode surface, not allow the hydrogen evolution reaction (HER) to occur, readily release the desired reduced product, be cheap, and be selective to one product. CO_2 electrolysers based on proton exchange membrane water electrolysers (PEMWE) are likely to be the most economical method for CO_2 reduction and was hence used in this study.[68]

Carbon, conducting polymers, and various metal compounds have been used as electrodes for energy conversion and storage devices.[73] The disadvantages of metal catalysts have been discussed previously and so organic compounds for use as catalysts will be briefly discussed with a focus on polyaniline and other nitrogen bearing materials.

Nitrogen based and carbon organic electrocatalysts have received much attention from the scientific community as alternatives to or supports for platinum group metal electrocatalysts. This, not only in the field of PEM based systems (fuel cells, water electrolysers, and CO_2RR) but in other energy storage media as well including supercapacitors, pseudocapacitors, and various batteries.[73]

Primary, secondary, and tertiary amines have been shown to have the ability to capture CO_2 from industry and fall under the group 'alkanolamines'[11,74]. Examples of primary alkanolamines include monoethanolamine (MEA) and 2-amino-2-methyl-1-propanol (AMP), secondary alkanolamines include diethanolamine (DEA) and di-isopropanolamine (DIPA), and tertiary alkanolamines exist of N-methyl-diethanolamine (MDEA) and triethanolamine (TEA). These have been used extensively as chemical absorbents in the removal of CO_2.[11,75]

Pyridine and pyridazine as electrocatalysts under acidic conditions (pyridinium and pyridazinium) have researchers divided. Some believe them to be an independent catalyst[76], whilst others believe them to be a co-catalyst,[77] in either case these nitrogen-bearing materials show activity towards CO_2RR. Another opinion is that pyridizinium has no effect on the reaction but rather the reduction of hydronium ions occurs due to the rapid dissociation of the acid.[78]

It then leads to the assumption that amines and other nitrogen-bearing materials may be used in CO_2RR, as they capture CO_2. Providing the intermediates are bound strongly enough to stay on the

electrocatalyst surface and the product is bound loosely enough to the electrocatalyst so that the product may be released.[79]

Since their discovery in 1960, conducting polymers have received much attention in energy storage, sensors and electrochromic devices.[80] This is because they have high conductivity and good capacitive properties. They are also much more affordable than their metal and platinum group metal counterparts.[73]

Bearing this in mind, polyaniline (PANI) was chosen as a suitable cathodic electrocatalytic material. It is one of the most interesting of the conducting polymers as it has the highest specific capacitance due to its ability for multi-redox reactions, good electronic properties and good protonation.[81] It exists in three different oxidation states, leucoemeraldine, emeraldine, and pernigraniline, all of which are all present as a mixture in electrodes. Of these, emeraldine has the highest stability and conductivity after protonation so it is expected that this state is in the majority.[82] PANI also has a myriad of nanostructure morphologies it can be synthesised to, depending on the technique used, accurate control of oxidising agents and/or additives[83,84] These different morphologies exhibit different properties which can be used to tune PANI as a cathodic electrocatalyst for CO_2RR.

Formic acid and formaldehyde are intermediates in one of the proposed reaction pathways of the reduction of CO_2 to methanol. The six e^-, six H^+ reaction is suggested to proceed via multiple single-electron transfers (that specifically involve the two e^- and four e^- reduced species) when run in organic systems:

$CO_2 + 2e^- + 2\ H^+ \leftrightarrow HCO_2H$

$HCO_2H + 2e^- + 2\ H^+ \leftrightarrow H_2CO$

$H_2CO + 2e^- + 2\ H^+ \leftrightarrow H_3COH$[85]

For CO_2RR on metal catalysts that have high overpotentials towards HER, the main products are formic acid and formate, these results suggest the reaction pathway given above is a possible realistic pathway for CO_2RR. Under mild hydrothermal conditions, sugars may be converted to formic acid in biomass utilisation. Formic acid has limited uses and as such further reduction to methanol and other valuable products is required.[86]

Formic acid was the focus of this study as the cell set-up was not suitable for CO_2 gaseous or aqueous experiments and this will be addressed in the future. Apart from this, as we know formic acid is expected to be an intermediate in the reduction of CO_2 to methanol, using this as a starting material will aid in understanding the mechanism of CO_2RR.

3.2.2. Results and Discussion

3.2.2.1. Field emission scanning electron microscopy

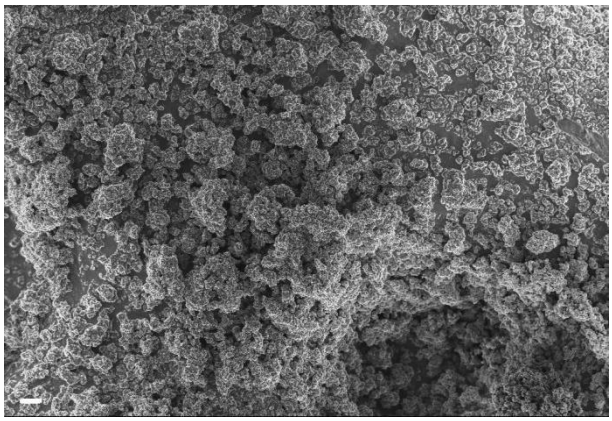

Figure 24: FESEM image of polyaniline powder. Size bar 10 µm

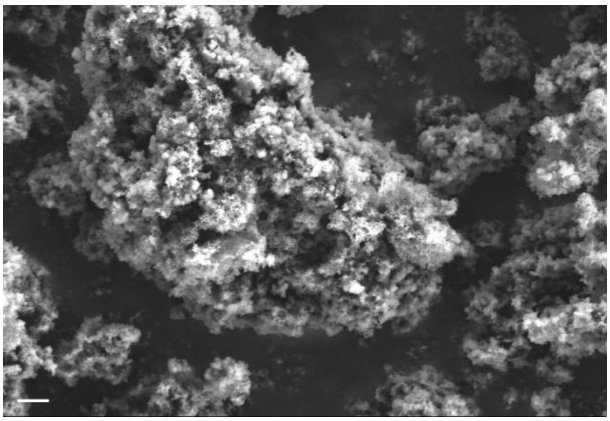

Figure 25: FESEM image of polyaniline powder, SE2 mode. Size bar 1 µm

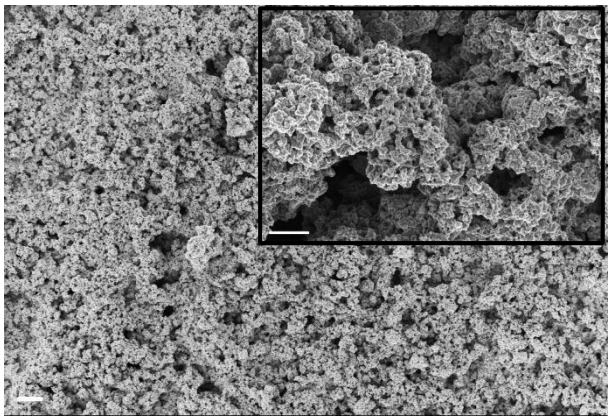

Figure 26: FESEM image of polyaniline coated membrane. Size bar 10 µm, inset size bar 1µm

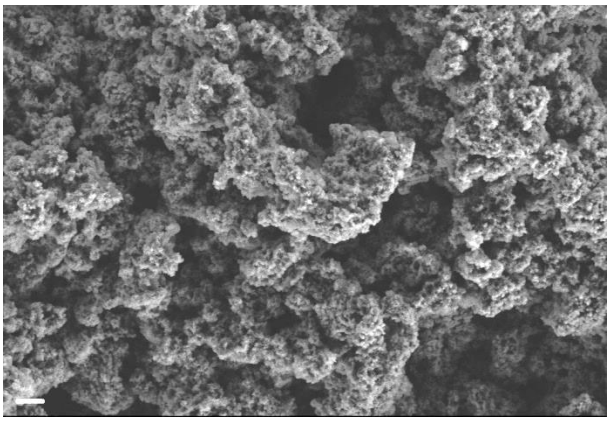

Figure 27: FESEM image of polyaniline coated membrane, SE2 mode. Size bar 2 µm

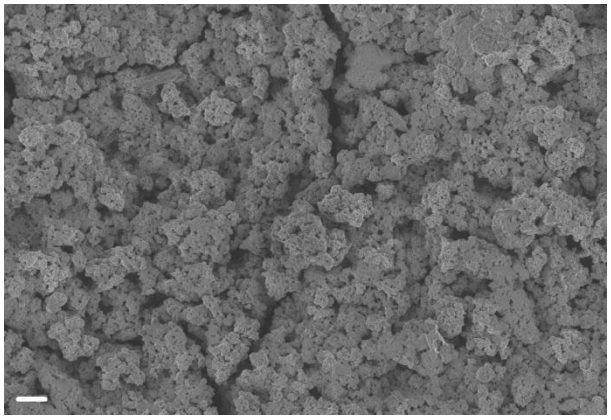

Figure 28: FESEM image of used polyaniline coated membrane.
Size bar 2 µm

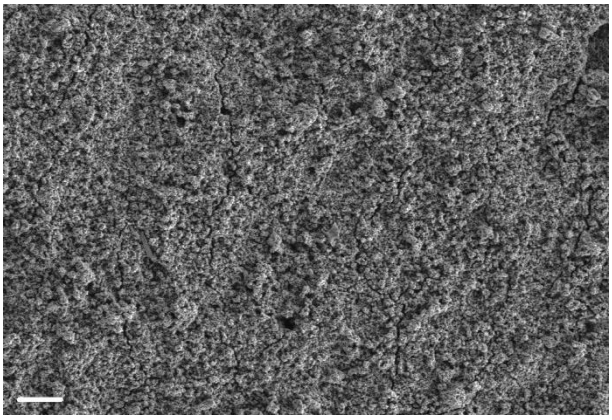

Figure 29: FESEM image of used polyaniline coated membrane, SE2 mode.
Size bar 20 µm

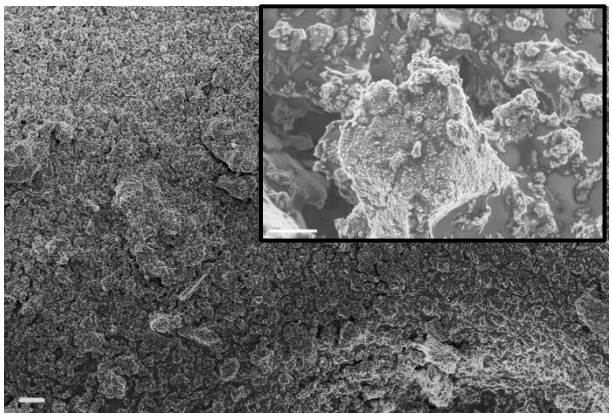

Figure 30: FESEM image of synthesised anode electrocatalytic powder.
Size bar 10 µm, inset size bar 1 µm

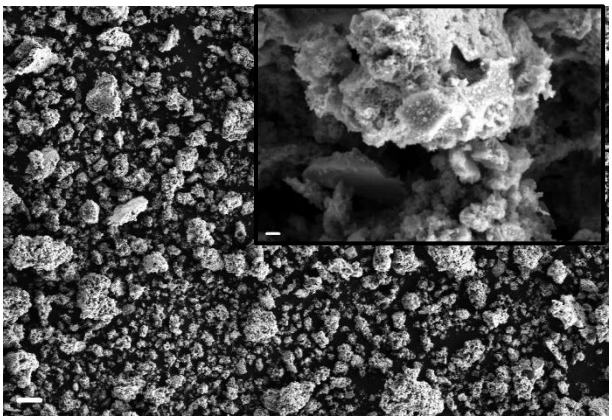

Figure 31: FESEM image of synthesised anode electrocatalytic powder, SE2 mode.
Size bar 10 µm, inset size bar 200nm

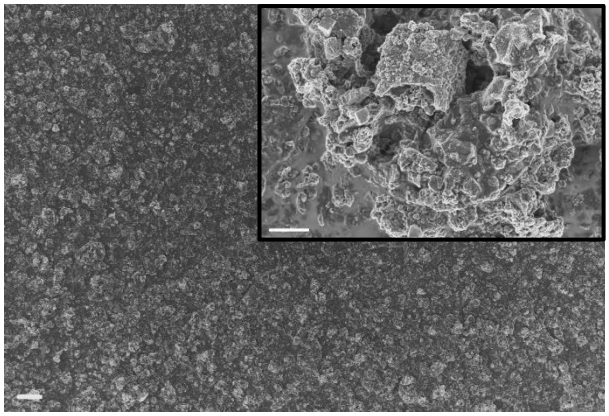

Figure 32: FESEM image of synthesised anode electrocatalytic powder coated membrane.
Size bar 10 µm, inset size bar 1 µm

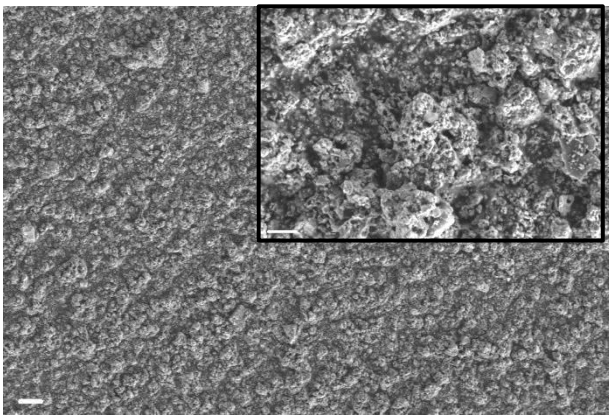

Figure 33: FESEM image synthesised anode electrocatalytic powder coated membrane, SE2 mode.
Size bar 10 µm, inset size bar 2 µm

Selected FESEM micrographs are shown above. Those on the left-hand side were taken using the standard in-lens detector whereas those on the right-hand side were taken in SE2 mode, using the Everhart-Thornley (ET) secondary electron detector. FESEM served to characterise the morphology of the PANI powder, the anodic and cathodic coated membranes, and the used PANI coated membranes. PANI was synthesised at the Chemical Engineering Department at the University of Pretoria. The powder was used as is for FESEM analysis but for the coated membranes the ink was prepared as described in Chapter 2, section 2.3 and a section of either unused or used catalyst coated membrane was cut out and stuck onto the double-sided carbon tape used for FESEM analysis (section 2.6.2).

Figures 24 and 25 are of the PANI powder, as observed the PANI particles are predominantly rectangular in shape with rounded edges in the range of 10 µm. A single PANI particle is shown in figure 25 and under the ET detector, it is clear the morphology of the particle is not smooth but rather has many little outgrowths. These outgrowths may be responsible for an increase in the surface area of the PANI particles and thereby enhancing its electrocatalytic activity, these are also observed in figure 27, the coated membrane. From what looked like a single particle in figure 24, now under higher magnification in figure 25 rather looks like an agglomeration of even smaller particles of various sizes. In figures 26 and 27 a better distribution of particles is observed once the ink has been coated on the membrane. The inset of figure 26 demonstrates that the PANI ink is self-similar, where the physical structure observed at higher magnification is the same as that at lower magnification. Figures 28 and 29 display the emergence of cracks along the coated surface of the used membrane which could have occurred during the runtime of the membrane, during disassembly, subsequent drying out of the membrane or due to wearing out of the sample. Both figures still show a uniform surface and in this regard are the same as the unused membrane. It is important to note, however, that two different membranes have been shown for the before and after use.

Figure 30 shows the morphology of the powder, and the insert is that of a large particle with smaller particles (possibly crystallites) attached to it, both figures 30 and 31 indicate that the powder has a rough surface. Figure 31 better shows the different particle sizes of the powder before preparation. Also, in SE2 mode small growths are visible on a particle that is part of an agglomeration. Again, better homogeneity both in size and distribution is observed on the electrocatalytic coated membrane in figures 32 and 33. But the inserts indicate that areas of agglomeration do still exist. Perhaps these agglomerations which result in heterogeneity could affect the efficiency of the

electrocatalyst. No visible differences were found between the used and unused membranes and they are therefore not shown here.

3.2.2.2. Electrochemical characterisation

3.2.2.2.1. Linear sweep voltammetry

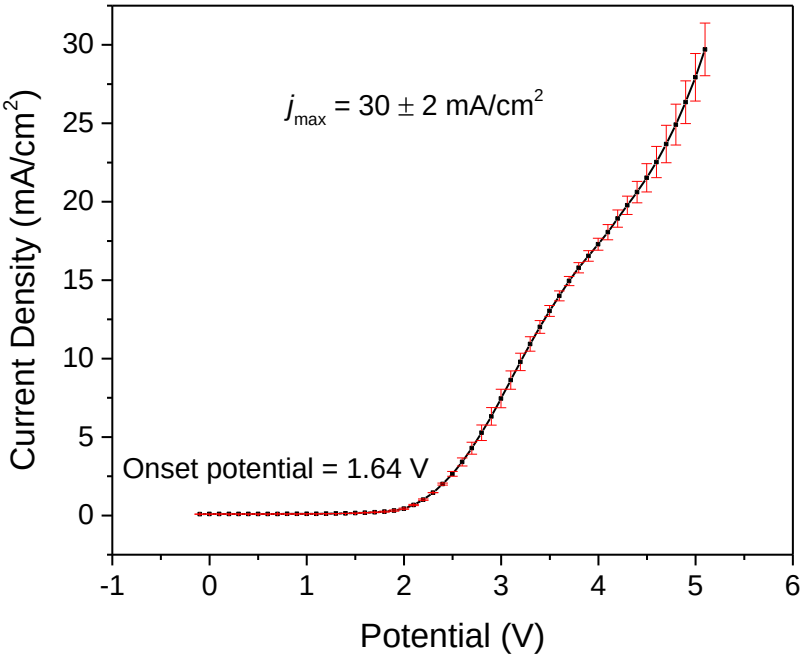

Figure 34: Linear sweep voltammogram for membrane B2 at a potential range of -0.1 to 5.1 V. The maximum current density is given at 5.1 V.

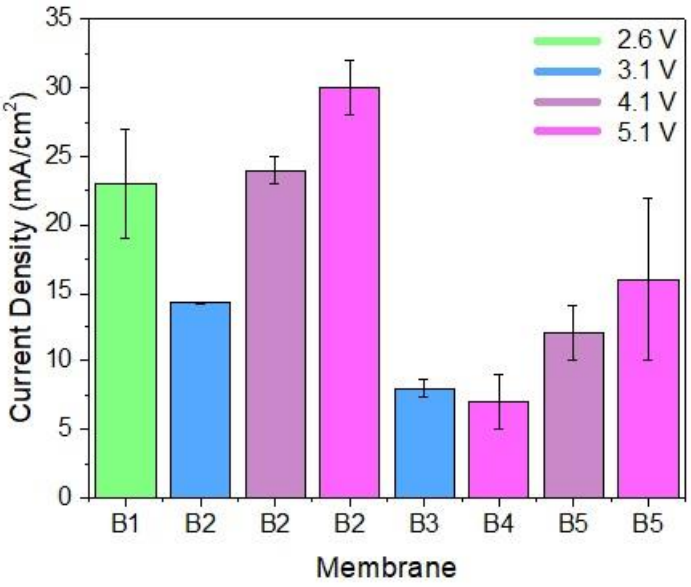

Figure 35: Bar graph illustrating the maximum current densities reached for each membrane at the maximum applied potentials where methanol was detected.

Of the nine membranes that were identically prepared (see Chapter 2), there were eight samples taken from test runs of five of the membranes that tested positive for methanol. These were all prepared with PANI as the cathode. The onset potential taken from all the linear sweep voltammograms (Figure 34 and Figures B1-B9 in Appendix B) ranges between 1.40 and 2.08 V (overpotential of 190 to 870 mV) which is quite a variation but shows that the preparation of the membranes may need to be improved upon. This can be done in future by ensuring a constant spray volume and pressure to determine exactly the amount of electrocatalyst that was deposited on the membrane and to keep it uniform. There is an error of human nature in these results because of the method used to determine the onset potential: a straight line was drawn in the initial part of the linear sweep voltammogram followed by another line drawn tangential to the graph as it deviated from linearity, where these lines intersect is the onset potential. Membrane B2 at 5.1 V produced the highest current density for LSV at 30 ± 2 mA/cm^2. Membrane B2 and B5 suggest that the current density increases with the applied potential.

3.2.2.2.2. Chronoamperometry

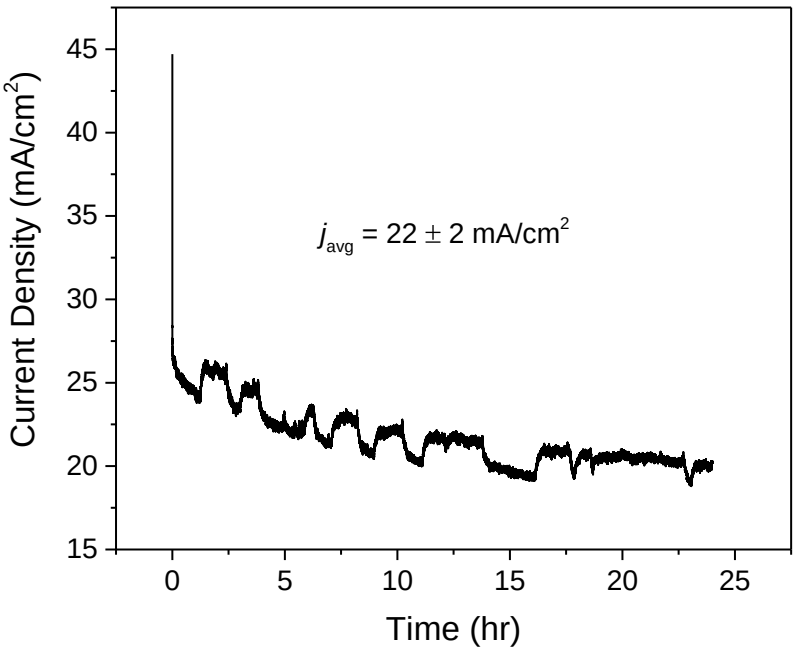

Figure 36: Chronoamperometry for membrane B2 at an applied potential of 5.1 V.

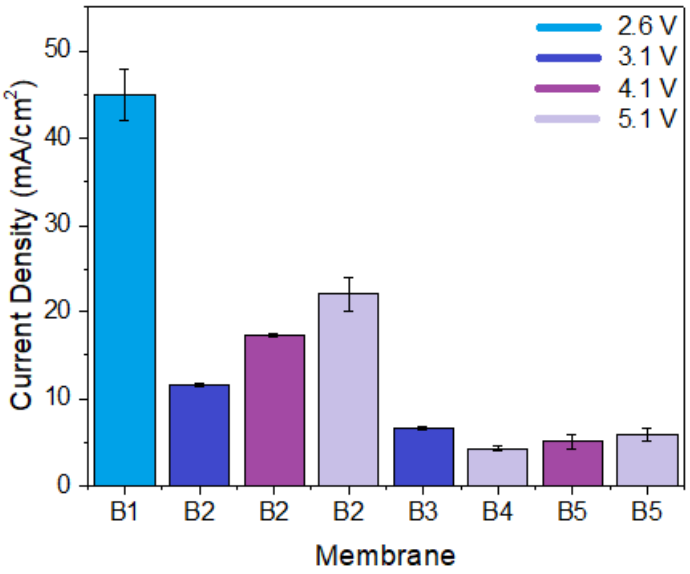

Figure 37: Bar graph of the average current densities during chronoamperometric runs at applied potentials described in the legend.

The chronoamperometric curve in Figure 36 indicates good stability of the membrane and is seen throughout the nine samples where methanol was detected (Figures B10-B18, Appendix B). This indicates no or very slow degradation of the electrocatalyst coated membrane during running time. It is thought that the drops in the current density are due to the HER where hydrogen occupies all the area in the serpentine groove and less formic acid is at the electrocatalytic surface. This would decrease the current density for CO_2RR momentarily until new formic acid flows to the electrocatalytic surface. In all membranes, there were no physical signs of damage to the membrane itself, once the cell was disassembled. These observations are in agreement with those made in the FESEM images above where no changes, except for minor cracks of unknown origin, were observed between the used and unused electrocatalyst coated membranes.

The bar graph indicates the average current densities throughout the chronoamperometric runs. Membrane B1 is the best performing membrane and again membrane B2 suggests an increased current density with applied potential. As observed in LSV it seems that a larger applied potential results in a higher maximum current density. Membrane B4 was by far the worst performing membrane of the lot yet even at such low current densities (4.3 ± 0.3 mA/cm^2) methanol was detected in the sample. This seems to suggest that a large current density is not a prerequisite for methanol formation. This is because there three kinds of reactions are monitored in the cell, namely, the oxygen evolution reaction, hydrogen evolution reaction and the reduction of formic acid. The water electrolysis and the methanol formation is expected to occur at similar applied voltages. Hence, the occurrence of a current produced (i.e. the current density observed) indicates there is a reaction occurring but it does not indicate which reaction is occurring. Therefore, although membrane B1 produced the largest current density it is, at this point, not possible to determine which of the reactions are contributing in the majority. Nevertheless, the product selectivity is a more crucial component than the current density produced.

3.2.2.3. Gas chromatography

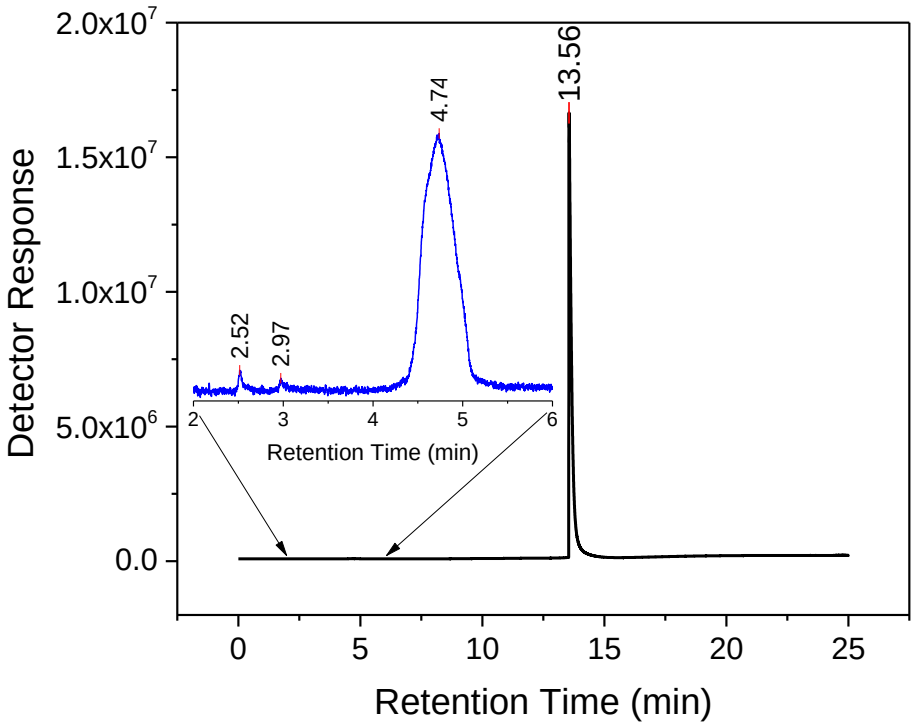

Figure 38: Chromatogram of sample B2 at 5.1 V.

In the chromatogram above, formic acid has a retention time of 13.56 min and if a section is taken from 2 to 6 minutes a clear peak is observed at 4.74 min for methanol. The retention times for methanol in all samples ranges from 4.62 to 4.97 min (Figures 38 and C1-C8, Appendix C). The variations were due to certain parameters being changed on the GC throughout the study. Some samples show peaks between 3 and 6 min, these peaks have not been classified as yet and their origin is unknown, however, the aim of the GC analyses was to detect methanol which was accomplished.

The first two peaks at 2.52 and 2.57 min are observed in every formic acid sample (even the standards) so this indicates either an impurity in the formic acid or a degradation product. It is assumed to be an impurity.

A number of gas samples were analysed by GC both during and after the running of the experiment. The results are not shown here as only hydrogen and small amounts of air were detected. This does, however, prove that the HER is very active in this system and a method to suppress it is required.

The concentration of methanol produced after a run and the faradaic efficiencies were calculated based on work carried out by Chen *et al*[87]. The concentration of methanol (%v/v) was determined using a calibration curve constructed from samples of known concentration of methanol in 15% formic acid from 0.0009 to 0.5% methanol. The peak area of the peaks from the gas chromatograms of the standard samples, corresponding to the methanol, was calculated using the Gaussian mode in Origin and plotted against the known concentration of the standards as shown in Figure 39, below. The R^2-value is 0.98911 which is appropriate to use the calibration curve to estimate the concentration of methanol in the unknown samples. In order to do this, the peak area was calculated for each methanol peak and, using the equation of the regression line a corresponding concentration was attained.

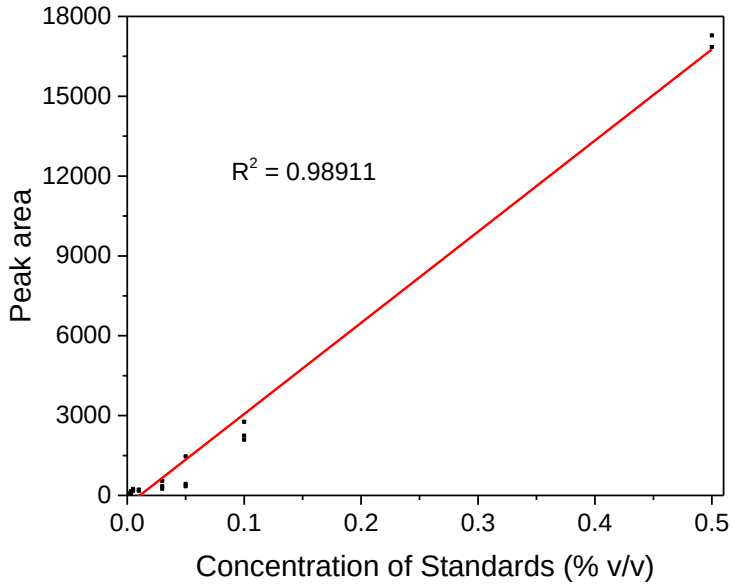

Figure 39: Analytical calibration curve using linear curve fit and residual plot

Table 8 below shows the concentration of methanol in each of the samples. The highest concentration of methanol was found in the sample obtained from membrane B2 at an applied voltage of 5.1 V of 0.1451 %v/v (0.7997 mmol methanol).

Table 8: Concentration of methanol in formic acid reduction samples

Membrane	**Concentration (%v/v)**	**Volume MeOH (mL)**	**mmol MeOH**
B1 at 2.6 V	0.0670	0.0134	0.3313
B2 at 3.1 V	0.0747	0.0170	0.4212
B2 at 4.1 V	0.1104	0.0244	0.6034

B2 at 5.1 V	0.1451	0.0324	0.7997
B3 at 3.1 V	0.0565	0.0109	0.2688
B4 at 5.1 V	0.0166	0.0034	0.0851
B5 at 4.1 V	0.0113	0.0021	0.0510
B5 at 5.1 V	0.0120	0.0023	0.0557

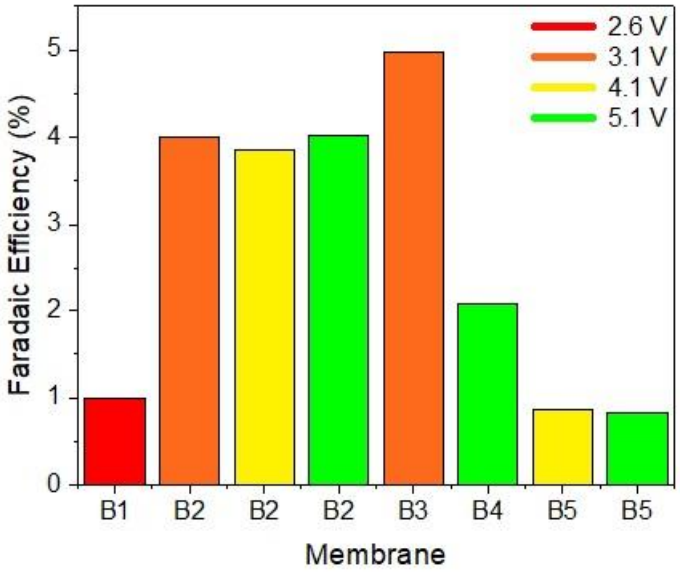

Figure 40: Faradaic efficiencies.

Figure 40 above shows the faradaic efficiency of methanol in each sample. Membrane B3 at an applied voltage of 3.1 V produced the highest faradaic efficiency (4.97%).The faradaic efficiency was calculated using equations 2, 3 and 4:

$$faradaic\ efficiency = \frac{e^-_{output}}{e^-_{input}} \quad \ldots 2$$

Where

$$e^-_{output} = product\ (mol) \times electrons\ required\ to\ produce\ 1\ mol\ product \quad \ldots 3$$

where the product (in mol) is taken from table 8, above, and the electrons required for 1 mol of product is four.

And

$$e^-_{input} = \frac{Q}{F} = \frac{I \times t}{F} \quad \ldots 4$$

where Q is the measured charge (C), I is the current (A), t is the time of the experiment (s), and F is Faraday's constant (C/mol). Hence the smaller the current, the larger the faradaic efficiency is.

Membrane B2 at 5.1 V produced the most methanol and it also exhibited the highest current density for LSV however only second highest current density for chronoamperometric experiments, where, it produced roughly half of the highest performing membrane (B1). This proves that the production of methanol may not necessarily rely on the current density produced by the sample but rather on product selectivity. The electrocatalyst is not yet entirely selective to one product as seen in some of the gas chromatograms by the appearance of peaks between 3 and 6 minutes.

Chapter 4 Conclusions and future work

4.1. Conclusions

Of the four anode powders tested for water electrolysis (100% IrO_2 commercial, 100% IrO_2 synthesised, 70:30 mol% IrO_2:TaC and 60:40 mol% IrO_2:TaC) 70:30 mol% IrO_2:TaC showed best catalytic activity in both linear sweep voltammetry and chronoamperometry. In both cases this composition had the highest current densities at stop potential and constant applied potential, respectively. The FESEM images show the emergence of a platy, vitreous-like phase in all the synthesised powders and any agglomerations had rounded rather than sharp edges. Both of these factors will have increased the surface area of the electrocatalyst and possibly allowed for enhanced catalytic activity.

Consequently, this anode electrocatalytic powder was used for all the formic acid reduction experiments. Eight samples throughout five of the nine prepared membranes proved positive for the reduction reaction of formic acid to methanol as tested by gas chromatographic analysis. For membranes B2 and B5, a higher applied potential resulted in a higher current density, and also an increase in the concentration (%v/v) of methanol. Membrane B2 at 5.1 V produced the highest concentration of methanol although it did not consistently produce the highest current densities. This suggests that the catalytic activity is not necessarily dependant on the current density produced.

There were unidentified peaks in some of the gas chromatograms whose origin has not been identified as of yet.

4.2. Future work

The faradaic efficiencies are good enough to warrant further investigation into this system. A better understanding of the mechanism can be gained by using applied electrochemical techniques, for example, cyclic voltammetry, rotating disk electrode, as well as DFT calculations. Understanding the mechanism by which this reaction runs will bring us closer to understanding the reaction mechanism of CO_2RR using an organic electrocatalyst.

Experiments using gaseous feedstock must also be done to test if this electrocatalyst is a viable one for CO_2RR. A gaseous carbon dioxide feedstock is preferable to an aqueous one as the latter would promote the HER.

The unknown peaks in the gas chromatograms need to be identified and quantified. Also it would be useful to have an on-line GC set up so that any products resulting from the reaction can be analysed in real time.

A more reproducible way of preparing the membranes needs to be identified in order to minimise uncertainties of the activities of the electrocatalysts. This method should also be quick and accurate.

References

(1) UNEP. UNFCCC COP 21 Paris France - 2015 Paris Climate Conference http://www.cop21paris.org/about/cop21 (accessed Jan 6, 2017).

(2) Department of Environmental Affairs. Summary of South Africa's position at CoP 21 - CMP 11 in Paris, France | Department of Environmental Affairs https://www.environment.gov.za/event/international/cop21cmp11_climatechange_paris_position (accessed Jan 6, 2017).

(3) WEC. *World Energy Counc. Rep.* **2016**, *1*, 468.

(4) Solomon, S.; Plattner, G.-K.; Knutti, R.; Friedlingstein, P. *Proc. Natl. Acad. Sci. U. S. A.* **2009**, *106* (6), 1704.

(5) Lorenz, K.; Crutzen, P. J.; Lal, R.; Töpfer, K. In *Recarbonization of the Biosphere: Ecosystems and the Global Carbon Cycle*; Lal, R., Lorenz, K., Hüttl, R. F., Schneider, B. U., von Braun, J., Eds.; Springer Netherlands: Dordrecht, 2012; pp 41–58.

(6) Goeppert, A.; Czaun, M.; Jones, J.-P.; Prakash, G. K. S.; Olah, G. A. *Chem. Soc. Rev.* **2014**, *43* (23), 7995.

(7) Shaftel, H. Climate Change: Vital Signs of the Planet: Carbon Dioxide http://climate.nasa.gov/vital-signs/carbon-dioxide/ (accessed Aug 7, 2016).

(8) NASA. Climate Change: Climate Resource Center - Graphic: Carbon dioxide hits new high http://climate.nasa.gov/climate_resources/7/ (accessed Jan 6, 2017).

(9) Olah, G. A.; Prakash, G. K. S.; Goeppert, A. *J. Am. Chem. Soc.* **2011**, *133* (33), 12881.

(10) Aresta, M.; Dibenedetto, A. *Dalton Trans.* **2007**, No. 28, 2975.

(11) Thambimuthu, K. Soltanieh, M.Abanades, J. Allam, R. Bolland, O. Davison, J. Feron, P. Goede, F. Herrera, A. Iijima, M. Jansen, D. Leites, I. Mathieu, P. Rubin, E. Simbeck, D. Warmuzinski, K. Wilkinson, M. Williams, R. Jaschik, M. Lyngfelt, A. Span, R. Tan, M. In *IPCC Special Report on Carbon dioxide Capture and Storage*; Metz, B. Davidson, O. de Coninck, H. Loos, M. and Meyer, L., Ed.; Cambridge University Press, UK: Cambridge, 2005; pp 105–178.

(12) Department of Energy. South African Energy Sector https://www.usea.org/sites/default/files/event-file/497/South_Africa_Country_Presentation.pdf (accessed Aug 17, 2016).

(13) Dibenedetto, A.; Angelini, A.; Stufano, P. *J. Chem. Technol. Biotechnol.* **2014**, *89* (3), 334.

(14) Hu, B.; Guild, C.; Suib, S. L. *J. CO2 Util.* **2013**, *1*, 18.

(15) Kothandaraman, J.; Goeppert, A.; Czaun, M.; Olah, G. A.; Prakash, G. K. S. *J. Am. Chem. Soc.* **2016**, *138* (3), 778.

(16) Olah, G. A. *Angew. Chemie Int. Ed.* **2005**, *44* (18), 2636.

(17) Chouhan, N. and L. R. In *Electrochemical Technologies for Energy Storage and Conversion*; Liu, R., Zhang, L., Sun, X., Liu, H. and Zhang, J., Ed.; Wiley-VCH Verlag & Co., 2012; pp 1–48.

(18) Polonský, J.; Mazúr, P.; Paidar, M.; Christensen, E.; Bouzek, K. *Int. J. Hydrogen Energy* **2014**, *39* (7), 3072.

(19) Eberle, U.; Felderhoff, M.; Schüth, F. *Angew. Chemie - Int. Ed.* **2009**, *48* (36), 6608.

(20) Coontz, R.; Hanson, B. *Science* **2004**, *305* (August), 2004.

(21) Eberle, U.; Felderhoff, M.; Sch, F. **2009**, 6608.

(22) Okada, Y.; Sasaki, E.; Watanabe, E.; Hyodo, S.; Nishijima, H. *Int. J. Hydrogen Energy* **2006**, *31* (10), 1348.

(23) Yolcular, S.; Olgun, Ö. *Energy Sources, Part A Recover. Util. Environ. Eff.* **2007**, *30* (4), 309.

(24) Rivera-Tinoco, R.; Farran, M.; Bouallou, C.; Auprêtre, F.; Valentin, S.; Millet, P.; Ngameni, J. R. *Int. J. Hydrogen Energy* **2016**, *41* (8), 4546.

(25) Al-Kalbani, H.; Xuan, J.; García, S.; Wang, H. *Appl. Energy* **2016**, *165*, 1.

(26) Energy-Density of Transport Fuels http://investorintel.com/wp-content/uploads/2015/09/Energy-Density.png (accessed Jan 8, 2017).

(27) OFFICE of ENERGY EFFICIENCY & RENEWABLE ENERGY. Hydrogen Storage | Department of Energy https://energy.gov/eere/fuelcells/hydrogen-storage (accessed Jun 8, 2017).

(28) Lu, Q.; Jiao, F. *Nano Energy* **2016**, *29*, 439.

(29) Zhu, D. D.; Liu, J. L.; Qiao, S. Z. *Adv. Mater.* **2016**, *28* (18), 3423.

(30) Bevilacqua, M.; Filippi, J.; Miller, H. a.; Vizza, F. *Energy Technol.* **2015**, *3* (3), 197.

(31) Millet, P.; Ngameni, R.; Grigoriev, S. A.; Fateev, V. N. *Int. J. Hydrogen Energy* **2011**, *36* (6), 4156.

(32) Harris, D. C. In *Quantitative Chemical Analysis*; Harris, D. C., Ed.; Craig Bleyer: New York, 2007; p AP 20-27.

(33) Mauritz, K. A.; Moore, R. B. *Chem. Rev.* **2004**, *104* (10), 4535.

(34) Luo, Z.; Chang, Z.; Zhang, Y.; Liu, Z.; Li, J. *Int. J. Hydrogen Energy* **2010**, *35* (7), 3120.

(35) Sun, L.; Ran, R.; Wang, G.; Shao, Z. *Solid State Ionics* **2008**, *179* (21), 960.

(36) Gutiérrez-Guerra, N.; Moreno-López, L.; Serrano-Ruiz, J. C.; Valverde, J. L.; de Lucas-Consuegra, A. *Appl. Catal. B Environ.* **2016**, *188*, 272.

(37) Felix, C.; Maiyalagan, T.; Pasupathi, S.; Bladergroen, B.; Linkov, V. *Micro Nanosyst.* **2012**, *4* (3), 186.

(38) Isaacs, M.; Armijo, F.; Ram, G.; Trollund, E.; Biaggio, S. R. *J. Mol. Catal. A Chem.* **2005**, *229* (1–2), 249.

(39) Kopljar, D.; Inan, A.; Vindayer, P.; Wagner, N.; Klemm, E. *J. Appl. Electrochem.* **2014**, *44* (10), 1107.

(40) Mahmood, M. N.; MAsheder, D.; Harty, C. J. *J. Appl. Electrochem.* **1987**, *17*, 1159.

(41) Polonský, J.; Petrushina, I. M.; Christensen, E.; Bouzek, K.; Prag, C. B.; Andersen, J. E. T.; Bjerrum, N. J. *Int. J. Hydrogen Energy* **2012**, *37* (3), 2173.

(42) Adams, R.; Shriner, R. L. *J. Am. Chem. Soc.* **1923**, *45* (9), 2171.

(43) Puthiyapura, V. K.; Pasupathi, S.; Basu, S.; Wu, X.; Su, H.; Varagunapandiyan, N.; Pollet, B.; Scott, K. *Int. J. Hydrogen Energy* **2013**, *38* (21), 8605.

(44) Weng, D. *J. Electrochem. Soc.* **1996**, *143* (4), 1260.

(45) Millet, P. (Universite P.-S. 11). In *Hydrogen Production by Electrolysis*; Godula-Jopek, A., Ed.; Wiley-VCH, 2015; pp 63–115.

(46) Trasatti, S. *Electrochim. Acta* **1991**, *36* (2), 225.

(47) Carmo, M.; Fritz, D. L.; Mergel, J.; Stolten, D. *Int. J. Hydrogen Energy* **2013**, *38* (12), 4901.

(48) Matsumoto, Y.; Sato, E. *Mater. Chem. Phys.* **1986**, *14* (5), 397.

(49) Damjanovic, A.; Dey, A.; Bockris, J. O. *Electrochim. Acta* **1966**, *113* (7), 739.

(50) Miles, M. H.; Thomason, M. A. *J. Electrochem. Soc.* **1976**, *123* (10), 1459.

(51) Kötz, R.; Stucki, S. *Electrochim. Acta* **1986**, *31* (10), 1311.

(52) Pauli, C. P. De; Trasatti, S. *J. Electroanal. Chem.* **2002**, *538–539*, 145.

(53) Mazúr, P.; Polonský, J.; Paidar, M.; Bouzek, K. *Int. J. Hydrogen Energy* **2012**, *37* (17), 12081.

(54) Inc., I. 5 Year Iridium Prices and Price Charts http://www.infomine.com/investment/metal-prices/iridium/5-year/ (accessed Apr 15, 2017).

(55) Zhao, J.; Liu, Y.; Quan, X.; Chen, S.; Zhao, H.; Yu, H. *Electrochim. Acta* **2016**, *204*, 169.

(56) Lin, Z.; Waller, G. H.; Liu, Y.; Liu, M.; Wong, C. P. *Carbon N. Y.* **2013**, *53*, 130.

(57) Cheng, N.; Liu, Q.; Tian, J.; Xue, Y.; Asiri, A. M.; Jiang, H.; He, Y.; Sun, X. *Chem. Commun.* **2015**, *51* (9), 1616.

(58) Zhao, Y.; Nakamura, R.; Kamiya, K.; Nakanishi, S.; Hashimoto, K. *Nat. Commun.* **2013**, *4*, 2390.

(59) De Pauli, C. P.; Trasatti, S. *J. Electroanal. Chem.* **1995**, *396* (1–2), 161.

(60) Terezo, A. J.; Bisquert, J.; Pereira, E. C.; Garcia-Belmonte, G. *J. Electroanal. Chem.* **2001**, *508* (1–2), 59.

(61) Ardizzone, S.; Bianchi, C. L.; Cappelletti, G.; Ionita, M.; Minguzzi, A.; Rondinini, S.; Vertova, A. *J. Electroanal. Chem.* **2006**, *589* (1), 160.

(62) Marshall, A. T.; Sunde, S.; Tsypkin, M.; Tunold, R. *Int. J. Hydrogen Energy* **2007**, *32* (13), 2320.

(63) Rubel, M.; Haasch, R.; Mrozek, P.; Wieckowski, A.; De Pauli, C.; Trasatti, S. *Vacuum* **1994**, *45* (4), 423.

(64) Morimitsu, M.; Otogawa, R.; Matsunaga, M. *Electrochim. Acta* **2000**, *46* (2–3), 401.

(65) Chen, G.; Chen, X.; Yue, P. L. *J. Phys. Chem. B* **2002**, *106* (17), 4364.

(66) Marshall, A.; Børresen, B.; Hagen, G.; Tsypkin, M.; Tunold, R. *Mater. Chem. Phys.* **2005**, *94* (2–3), 226.

(67) Rasten, E.; Hagen, G.; Tunold, R. *Electrochim. Acta* **2003**, *48* (25–26), 3945.

(68) Jones, J. P.; Prakash, G. K. S.; Olah, G. A. *Isr. J. Chem.* **2014**, *54* (10), 1451.

(69) Speakman, S. A. 2014,.

(70) Aslibeiki, B.; Kameli, P.; Ehsani, M. H.; Salamati, H.; Muscas, G.; Agostinelli, E.; Foglietti, V.; Casciardi, S.; Peddis, D. *J. Magn. Magn. Mater.* **2016**, *399*, 236.

(71) Holzwarth, U.; Gibson, N. *Nat. Nanotechnol.* **2011**, *6* (9), 534.

(72) Ungár, T. *Scr. Mater.* **2004**, *51* (8 SPEC. ISS.), 777.

(73) Wang, H.; Lin, J.; Shen, Z. X. *J. Sci. Adv. Mater. Devices* **2016**, *1* (3), 225.

(74) Chowdhury, F. A.; Yamada, H.; Higashii, T.; Goto, K.; Onoda, M. *Ind. Eng. Chem. Res.* **2013**, *52* (24), 8323.

(75) Abu-Arabi, M. K.; Tamimi, A.; Al-Jarrah, A. M. *J. Chem. Eng. Data* **2001**, *46* (5), 1125.

(76) Apaydin, D. H.; Schlager, S.; Portenkirchner, E.; Sariciftci, N. S. *ChemPhysChem* **2017**, *18* (June), 1.

(77) Portenkirchner, E.; Enengl, C.; Enengl, S.; Hinterberger, G.; Schlager, S.; Apaydin, D.; Neugebauer, H.; Knör, G.; Sariciftci, N. S. *ChemElectroChem* **2014**, *1* (9), 1543.

(78) Costentin, C.; Canales, J. C.; Haddou, B.; Savéant, J. M. *J. Am. Chem. Soc.* **2013**, *135* (47), 17671.

(79) Zhang, Y.-J.; Sethuraman, V.; Michalsky, R.; Peterson, A. A. *ACS Catal.* **2014**, *4* (10), 3742.

(80) Bhadra, S.; Khastgir, D.; Singha, N. K.; Lee, J. H. *Prog. Polym. Sci.* **2009**, *34* (8), 783.

(81) Silva, C. H. B.; Galiote, N. A.; Huguenin, F.; Teixeira-Neto, É.; Constantino, V. R. L.; Temperini, M. L. a. *J. Mater. Chem.* **2012**, *22* (28), 14052.

(82) De Oliveira-Sousa, A.; Da Silva, M. A. S.; Machado, S. A. S.; Avaca, L. A.; De Lima-Neto, P. *Electrochim. Acta* **2000**, *45* (27), 4467.

(83) Amarnath, C. A.; Kim, J.; Kim, K.; Choi, J.; Sohn, D. *Polymer (Guildf).* **2008**, *49* (2), 432.

(84) Tran, H. D.; D'Arcy, J. M.; Wang, Y.; Beltramo, P. J.; Strong, V. A.; Kaner, R. B. *J. Mater. Chem.* **2011**, *21* (11), 3534.

(85) Cole, E. B.; Lakkaraju, P. S.; Rampulla, D. M.; Morris, A. J.; Abelev, E.; Bocarsly, A. B. *J. Amercian Chem. Soc.* **2010**, No. 12, 11539.

(86) Kotoulas, I.; Schizodimou, A.; Kyriacou, G. *Bentham Sci.* **2013**, *4*, 8.

(87) Chen, C. S.; Handoko, A. D.; Wan, J. H.; Ma, L.; Ren, D.; Yeo, B. S. *Catal. Sci. Technol.* **2015**, *5* (1), 161.

Appendix A SEM-EDX map sum spectra

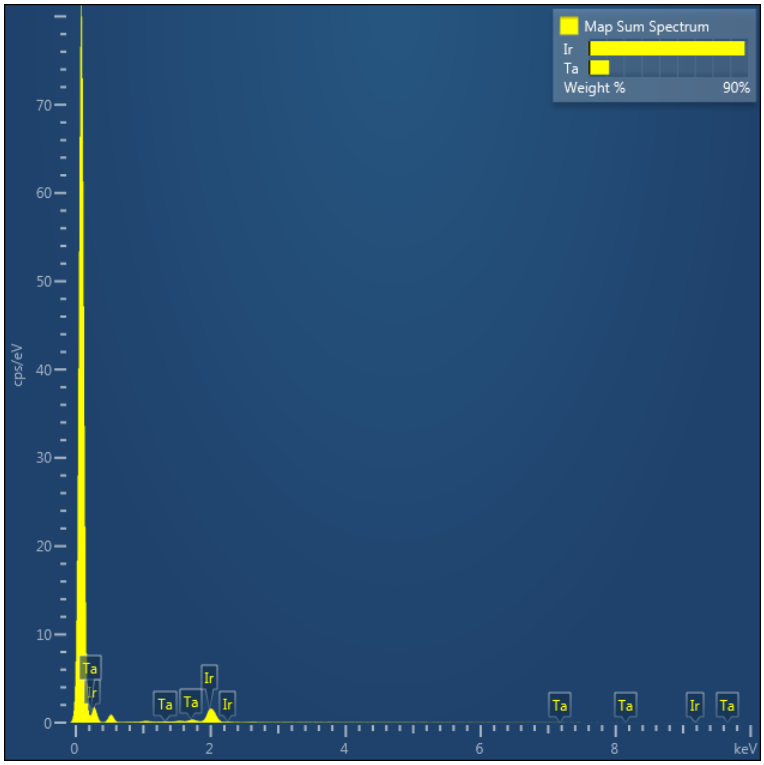

Figure A 1 Map sum spectrum of 60:40 mol% IrO_2:TaC showing surface enrichment of 90% Ir.

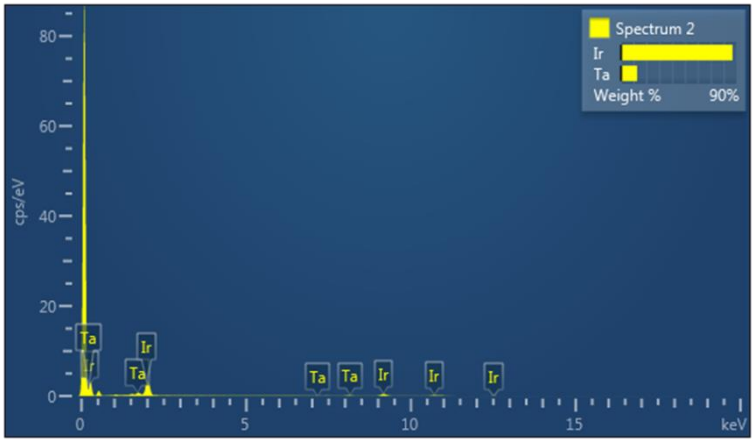

Figure A 2 Map sum spectrum for 70:30 mol% IrO_2:TaC showing surface enrichment of 90% Ir.

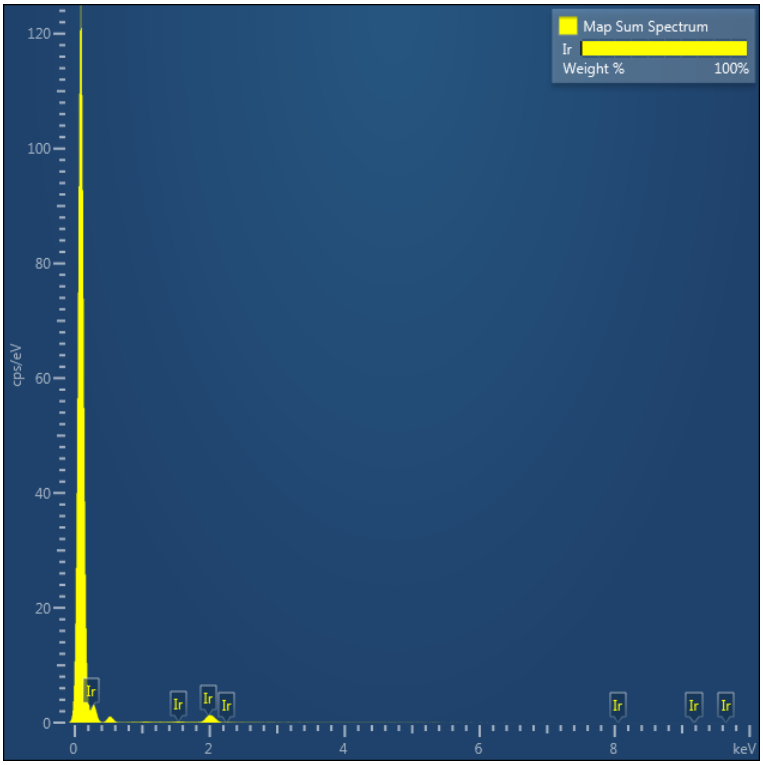

Figure A 3 Map sum spectrum for 100% synthesised IrO_2

Appendix B Electrochemical experimental curves

Linear sweep voltammetry (LSV)

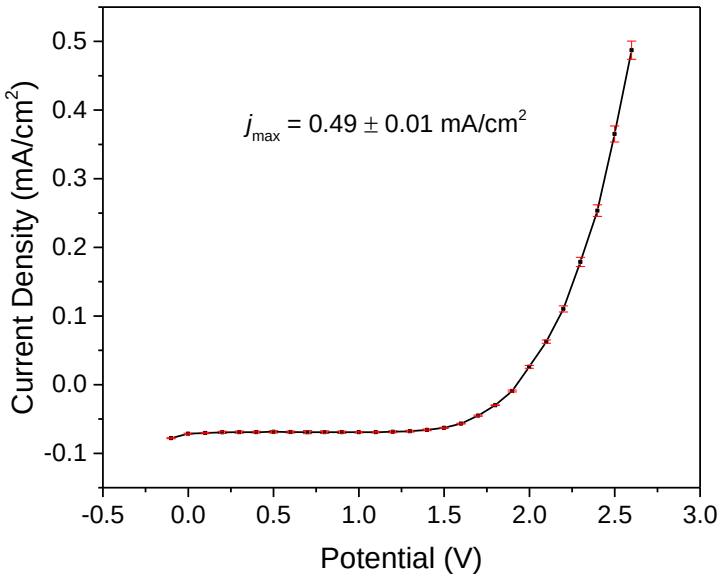

Figure B 1 LSV curve for membrane B with a stop potential of 2.6 V and an onset potential of 1.48 V.

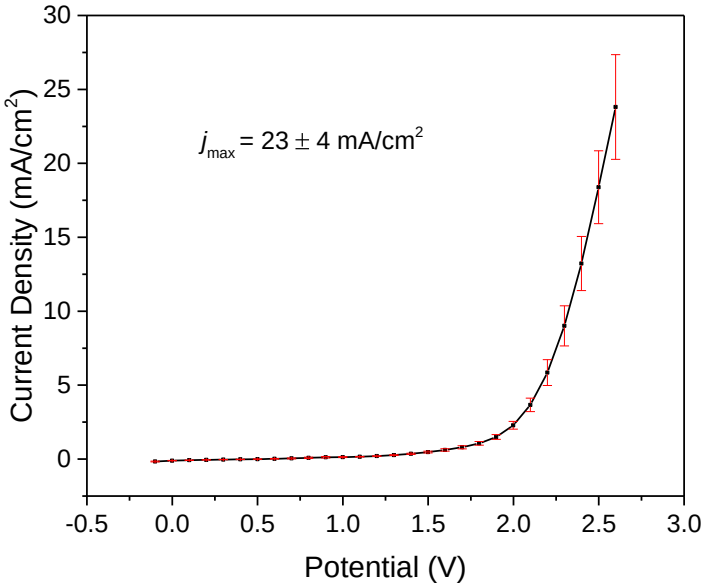

Figure B 2 LSV curve for membrane B1 with a stop potential of 2.6 V and an onset potential of 1.40 V

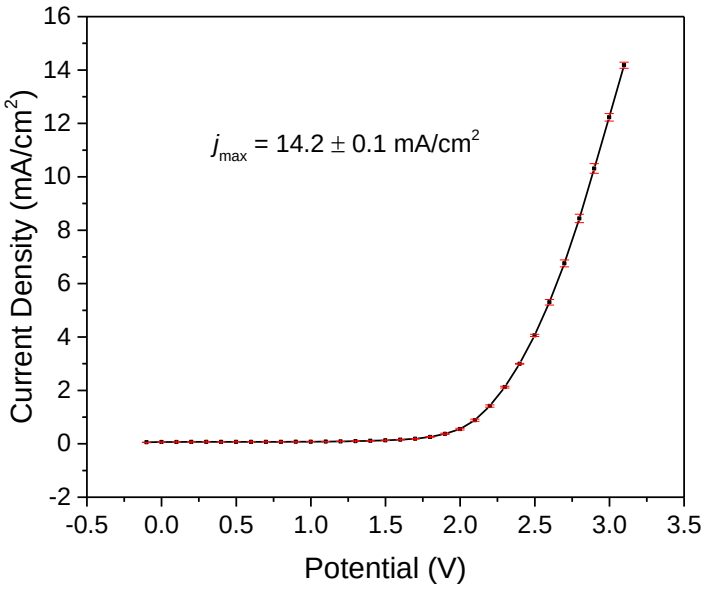

Figure B 3 LSV curve for membrane B2 with a stop potential of 3.1 V and an onset potential of 1.45 V.

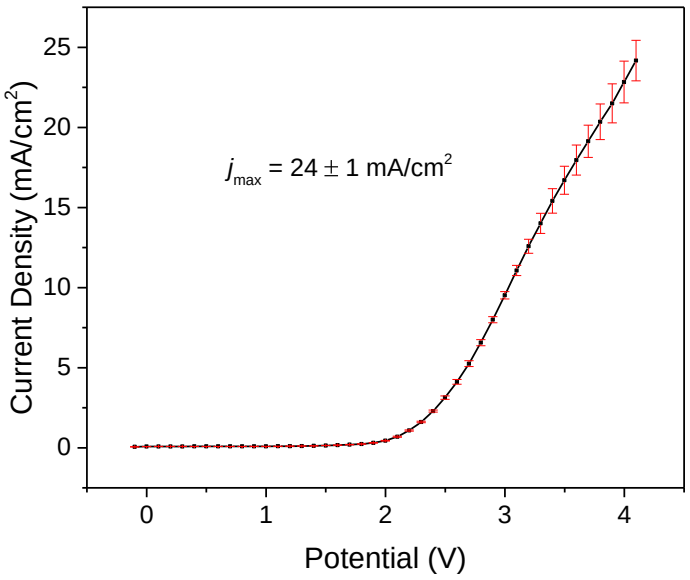

Figure B 4 LSV curve for membrane B2 with a stop potential of 4.1 V and an onset potential of 1.60 V.

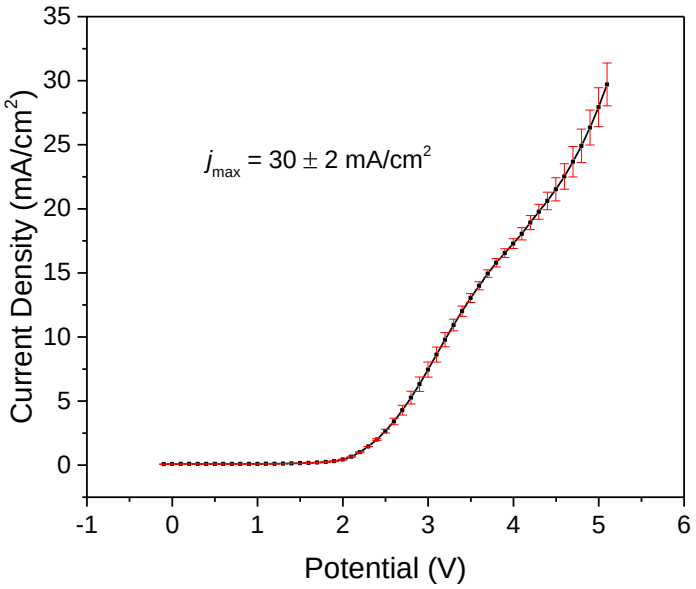

Figure B 5 LSV curve for membrane B2 with a stop potential of 5.1 V and an onset potential of 1.64 V.

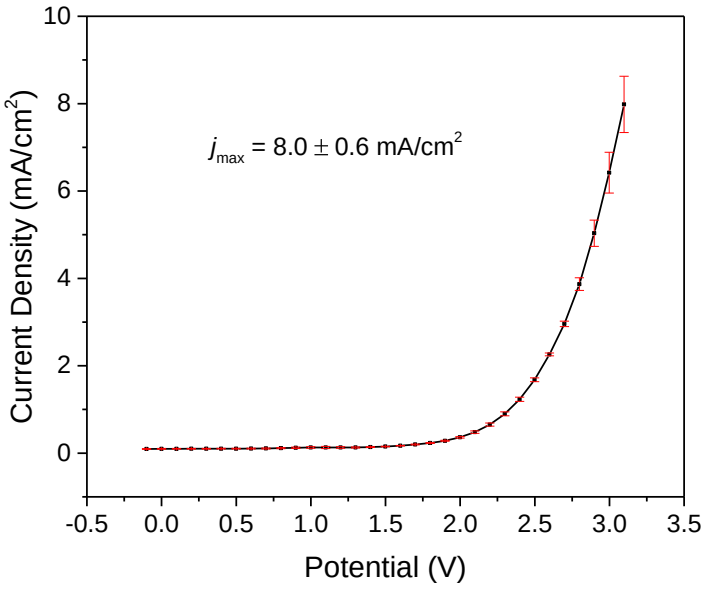

Figure B 6 LSV curve for membrane B3 with a stop potential of 3.1 V and an onset potential of 1.50 V.

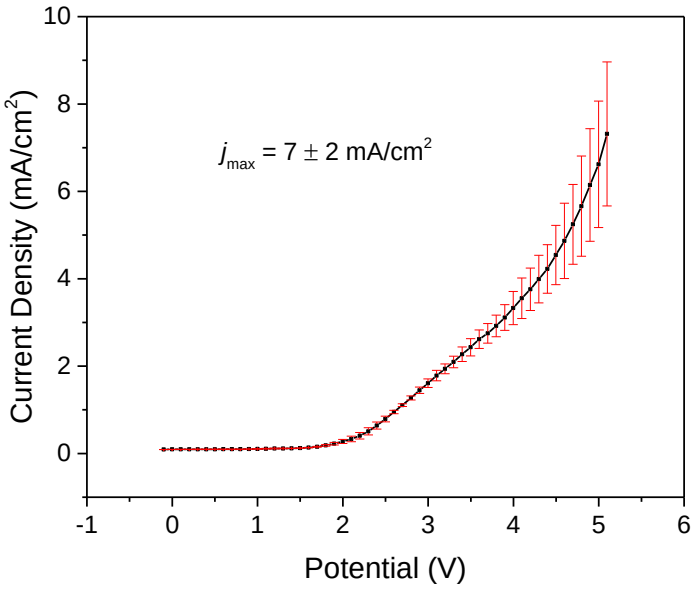

Figure B 7 LSV curve for membrane B4 with a stop potential of 5.1 V and an onset potential of 1.61 V.

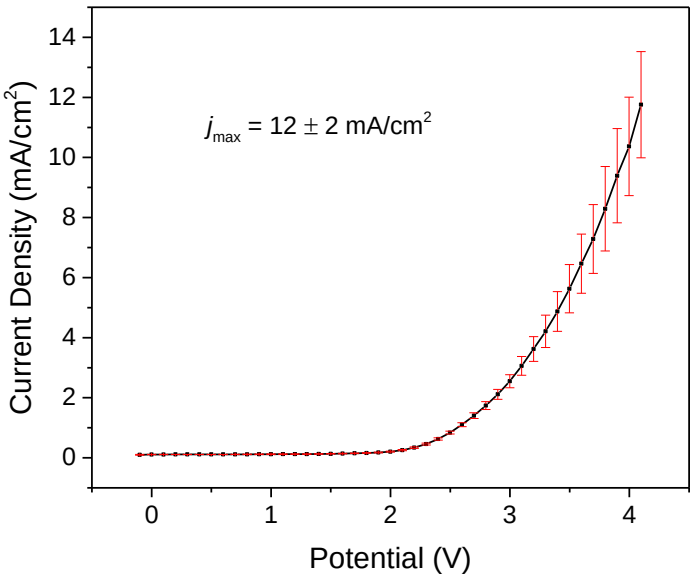

Figure B 8 LSV curve for membrane B5 with a stop potential of 4.1 V and an onset potential of 1.75 V.

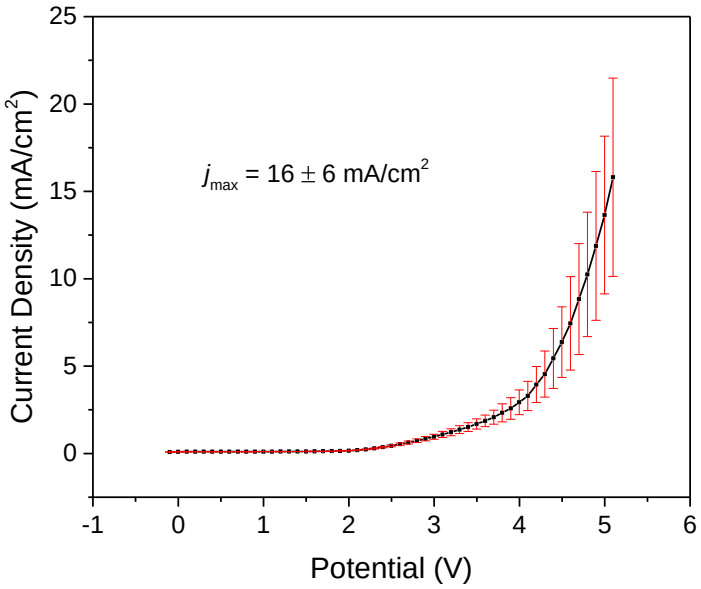

Figure B 9 LSV curve for membrane B5 with a stop potential of 5.1 V and an onset potential of 2.08 V.

Chronoamperometry (CA)

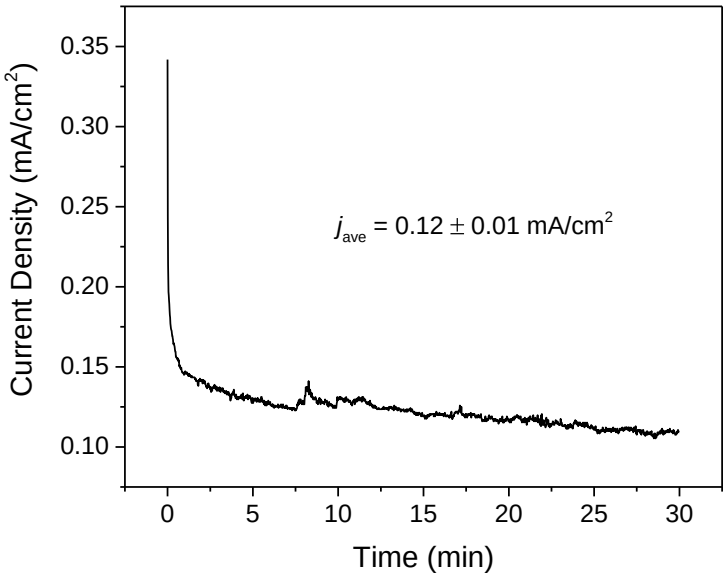

Figure B 10 CA curve of membrane B at an applied potential of 2.6 V over a period of 30 minutes.

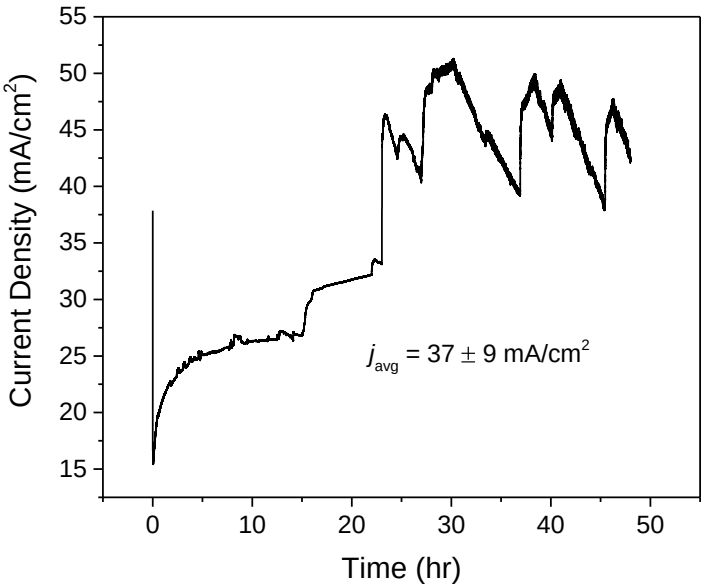

Figure B 11 CA curve of membrane B1 at an applied potential of2.6 V over a period of 48 hours.

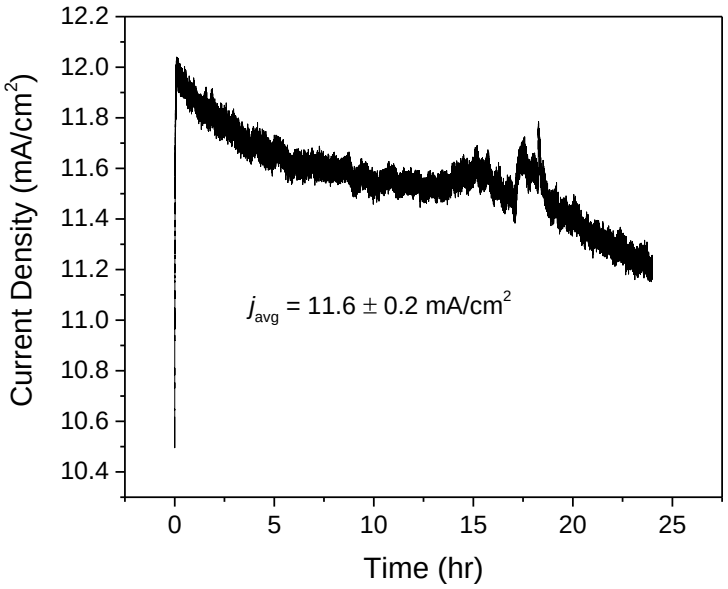

Figure B 12 CA curve of membrane B2 at an applied potential of 3.1 V over a period of 25 hours.

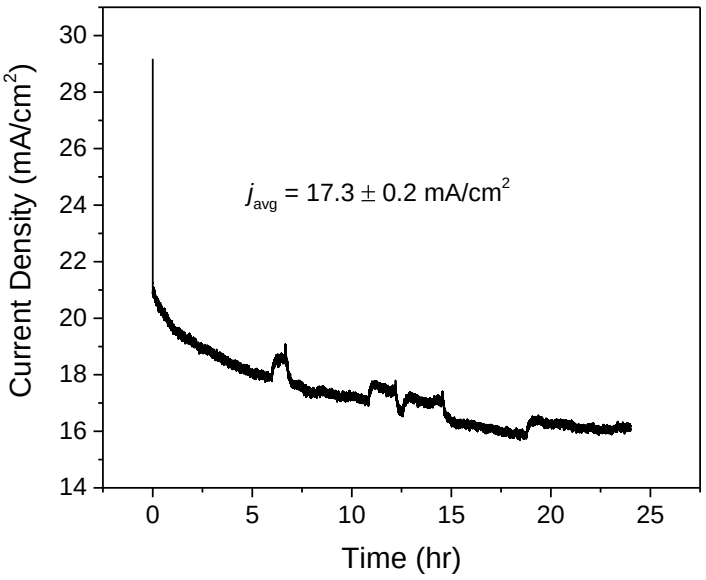

Figure B 13 CA curve of membrane B2 at an applied potential of 4.1 V over a period of 24 hours.

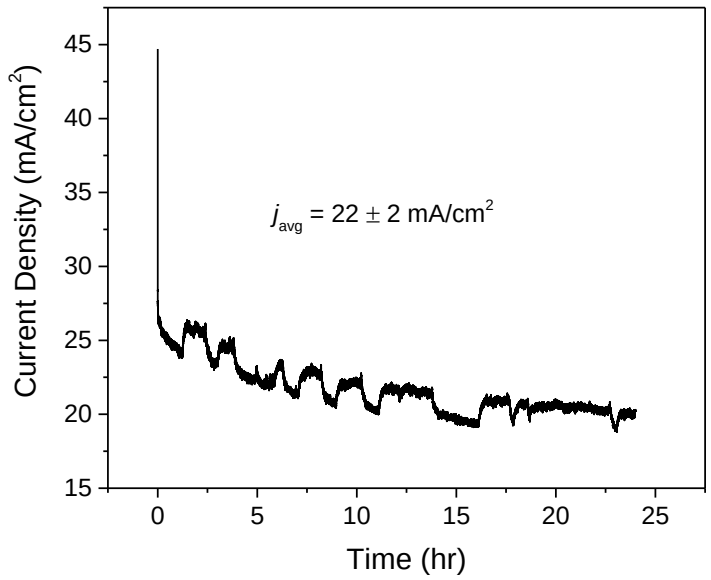

Figure B 14 CA curve of membrane B2 at an applied potential of 5.1 V over a period of 24 hours.

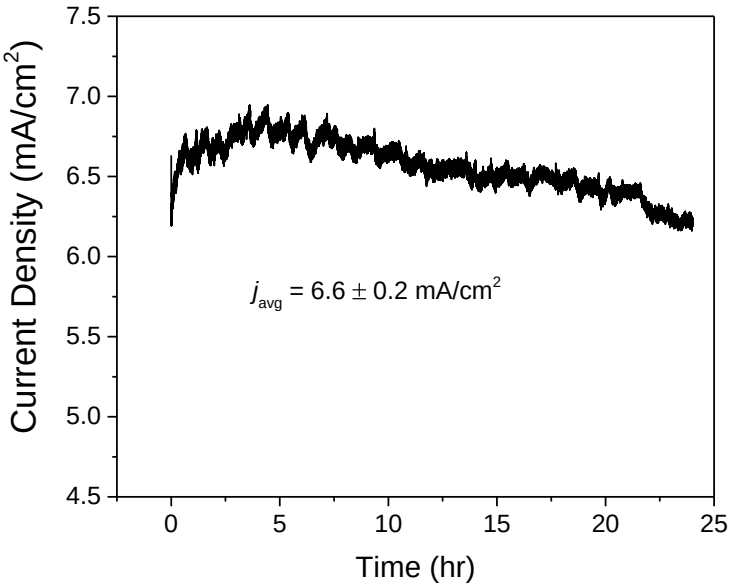

Figure B 15 CA curve of membrane B3 at an applied potential of 3.1 V over a period of 24 hours.

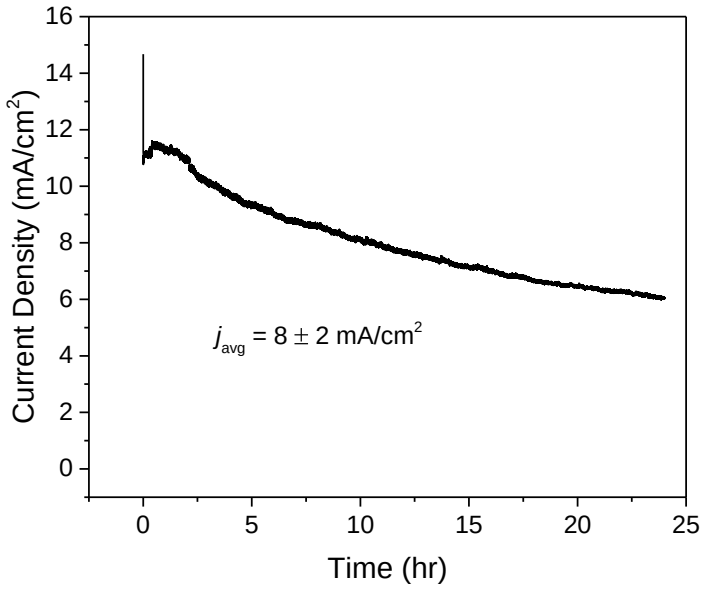

Figure B 16 CA curve of membrane B4 at an applied potential of 5.1 V over a period of 24 hours.

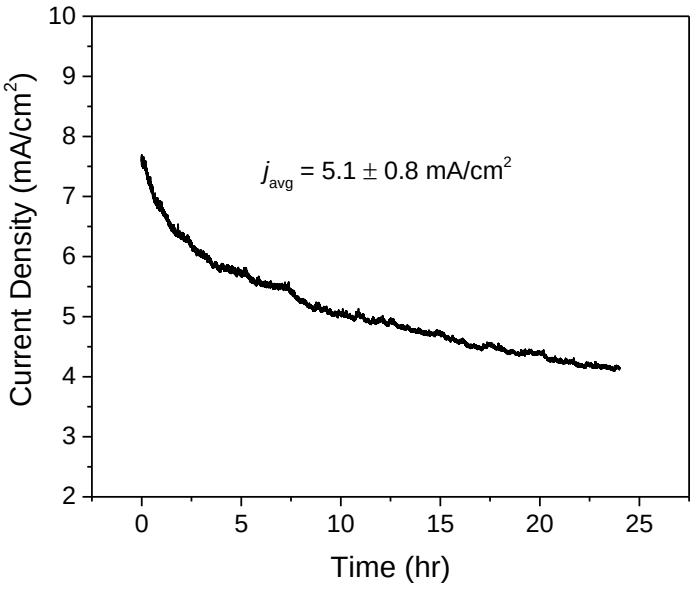

Figure B 17 CA curve of membrane B5 at an applied potential of 4.1 V over a period of 24 hours.

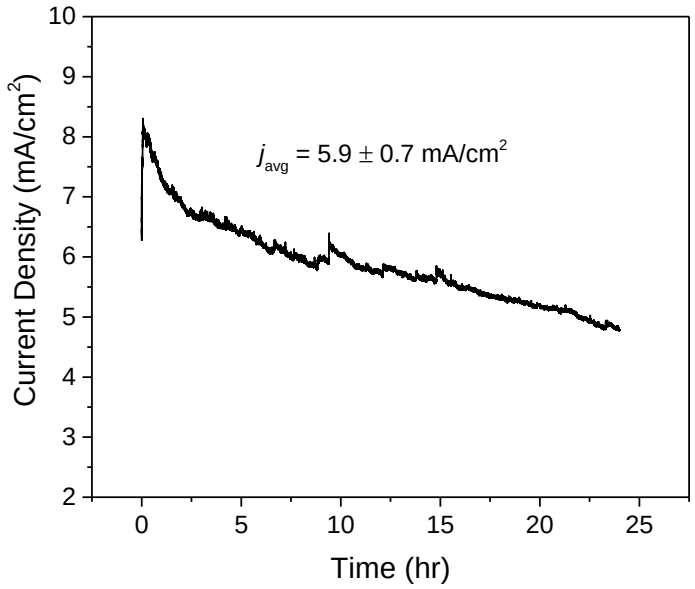

Figure B 18 CA curve of membrane B5 at an applied potential of 5.1 V over a period of 24 hours.

Appendix C Gas Chromatograms

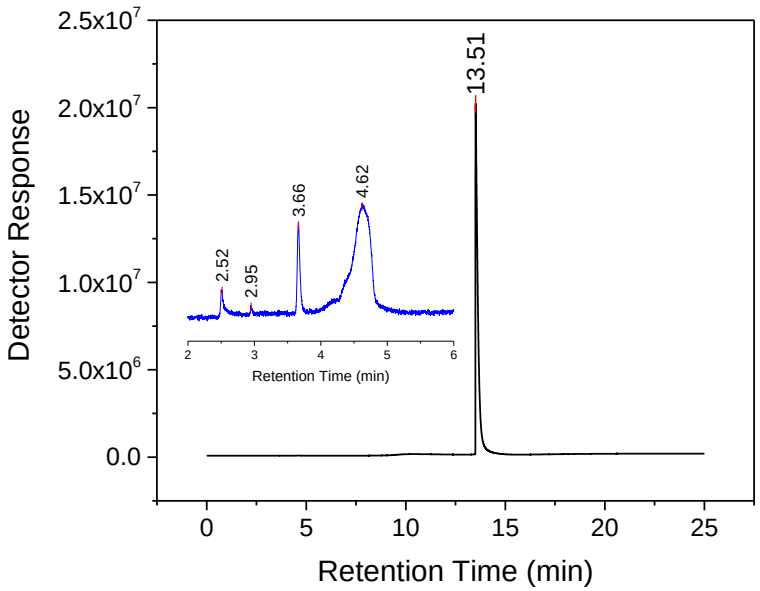

Figure C 1 GC graph of membrane B1 with a methanol peak at 4.62 min.

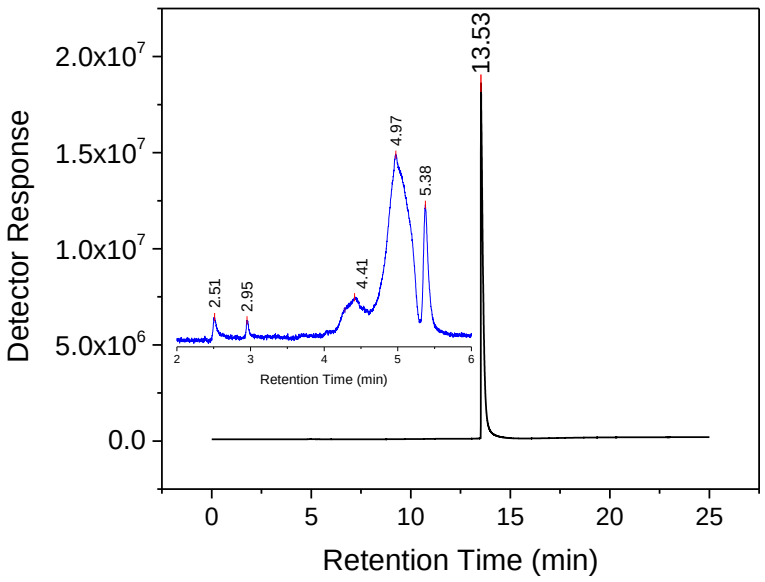

Figure C 2 GC graph of membrane B2_ 3.1 V with a methanol peak at 4.97 min.

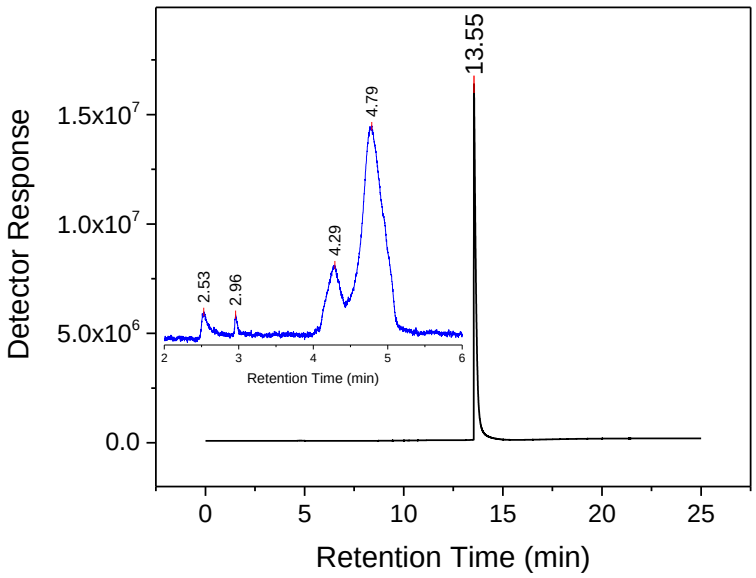

Figure C 3 GC graph of membrane B2_ 4.1 V with a methanol peak at 4.79 min.

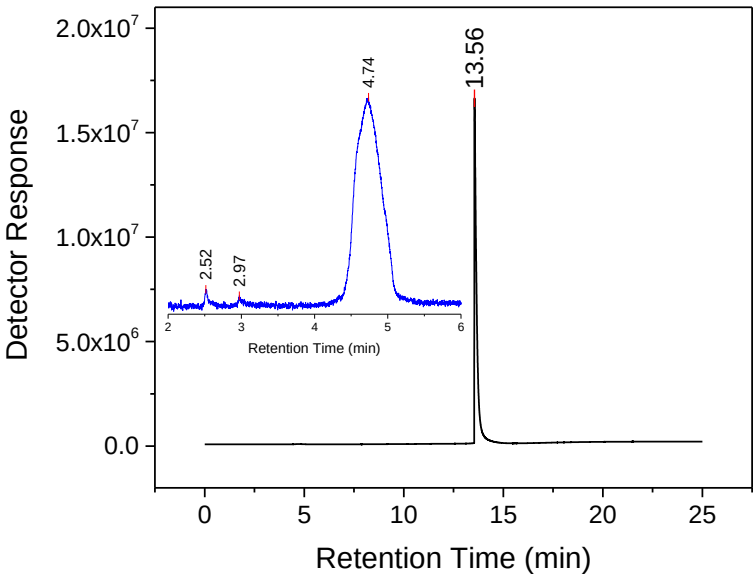

Figure C 4 GC graph of membrane B2_ 5.1 V with a methanol peak at 4.74 min.

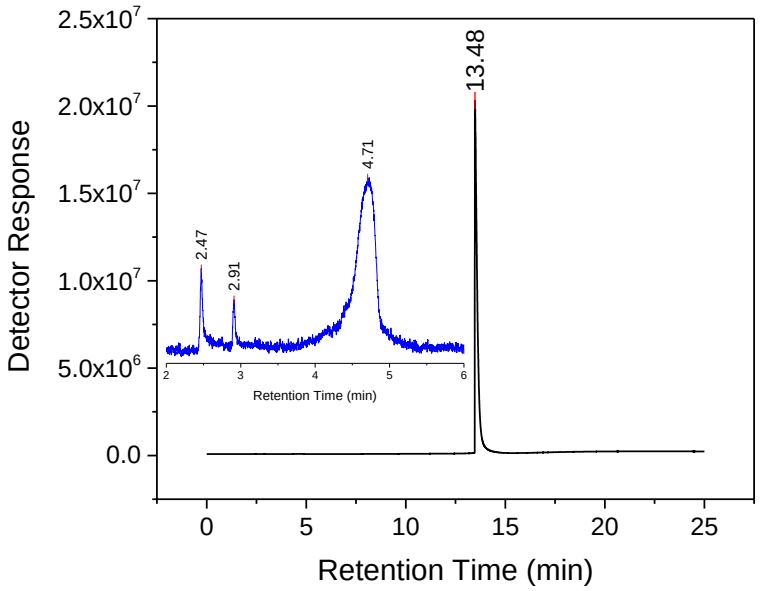

Figure C 5 GC graph of membrane B3 with a methanol peak at 4.71 min.

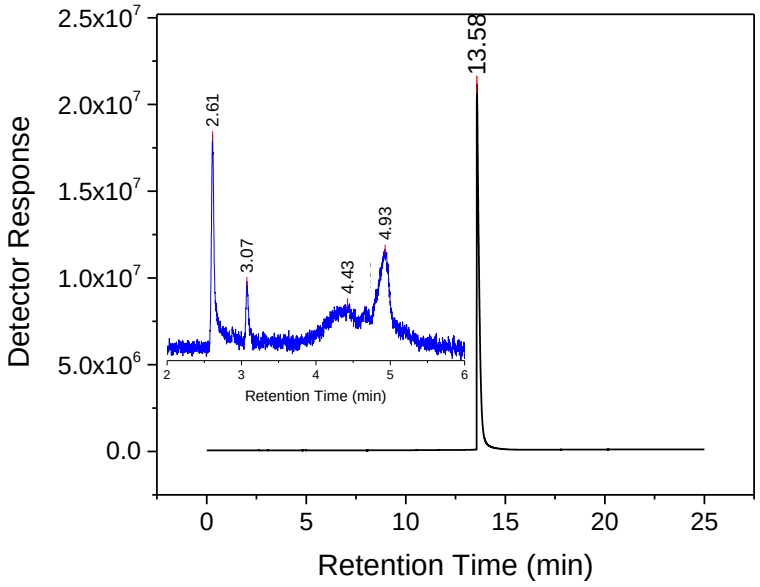

Figure C 6 GC graph of membrane B4 with a methanol peak at 4.93 min.

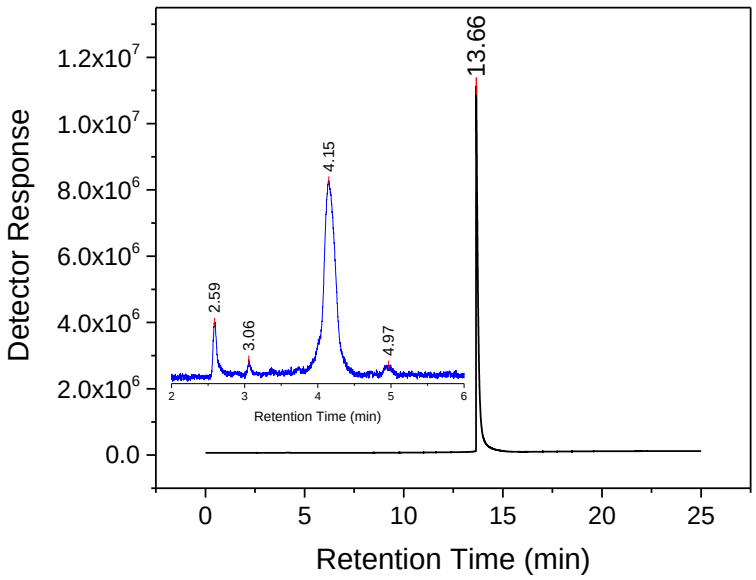

Figure C 7 GC graph of membrane B5_4.1 V with a methanol peak at 4.93 min.

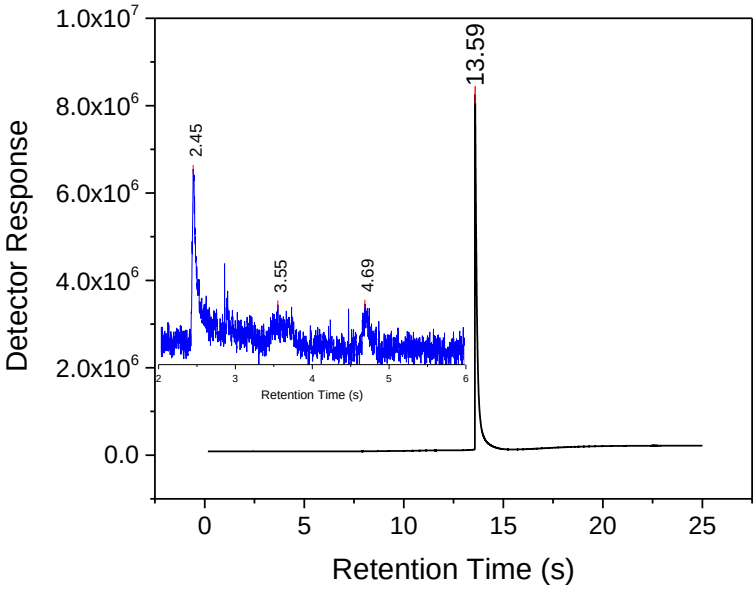

Figure C 8 GC graph of membrane B5_5.1 V with a methanol peak at 4.69 min.